AGU PUBLICATIONS

JGR

Journal of Geophysical Research: Solid Earth

RESEARCH ARTICLE
10.1002/2014JB011483

Key Points:
- Creep in the upper part of the EPF
- Key GNSS data for the NE Venezuela
- Identification of a compliant zone and rigidity contrast associated to the EPF

Correspondence to:
C. Reinoza,
creinoza@funvisis.gob.ve

Citation:
Reinoza, C., F. Jouanne, F. A. Audemard, M. Schmitz, and C. Beck (2015), Geodetic exploration of strain along the El Pilar Fault in northeastern Venezuela, *J. Geophys. Res. Solid Earth*, *120*, 1993–2013, doi:10.1002/2014JB011483.

Received 23 JUL 2014
Accepted 11 FEB 2015
Accepted article online 16 FEB 2015
Published online 30 MAR 2015

Geodetic exploration of strain along the El Pilar Fault in northeastern Venezuela

C. Reinoza[1,2], F. Jouanne[1], F. A. Audemard[2], M. Schmitz[2], and C. Beck[1]

[1]Université de Savoie Mont Blanc, ISTerre, Le Bourget du Lac, France, [2]Venezuelan Foundation for Seismological Research, Caracas, Venezuela

Abstract We use Global Navigation Satellite Systems observations in northeastern Venezuela to constrain the El Pilar Fault (EPF) kinematics and to explore the effects of the variable elastic properties of the surrounding medium and of the fault geometry on inferred slip rates and locking depth. The velocity field exhibits an asymmetric velocity gradient on either side of the EPF. We use five different approaches to explore possible models to explain this asymmetry. First, we infer a 1.6 km locking depth using a classic elastic half-space dislocation model. Second, we infer a 1.5 km locking depth and a 0.33 asymmetry coefficient using a heterogeneous asymmetric model, including contrasting material properties on either side of a vertical fault, suggesting that the igneous-metamorphic terranes on the northern side are ~2 times more rigid than the sedimentary southern side. Third, we use a three-dimensional elastostatic model to evaluate the presence of a compliant zone, suggesting a 30% reduction of rigidity in the upper 3 km at the depth of a 1 to 5 km wide fault zone. Fourth, we evaluate the distribution of fault slip, revealing a widespread partial creep pattern in the eastern upper segment, while the upper western segment exhibits a partially locked area, which coincides with the rupture surface of the 1797 and 1929 earthquakes. To supplement these models, we upgrade the previously published displacement simulation method using nonvertical dislocations with data acquired between 2003 and 2013. The localized aseismic displacement pattern associated with creeping or partially creeping fault segments could explain the low level of historic seismicity.

1. Introduction

Interpretations of Global Navigation Satellite System (GNSS) velocity fields across active strike-slip faults around the world allow determination of mechanical properties of the crust. Geodetic exploration has contributed to (i) the study of asymmetric velocity gradients related to the spatially variable mechanical properties of the crust [e.g., *Le Pichon et al.*, 2005; *Jolivet et al.*, 2008, 2009; *Houlié and Romanowicz*, 2011], (ii) confirmation of the existence of damage fault zones [e.g., *Chen and Freymueller*, 2002; *Fialko et al.*, 2002; *Fialko*, 2004; *Hamiel and Fialko*, 2007; *Barbot et al.*, 2009], and (iii) identification of partial or complete aseismic displacement [e.g., *Bürgmann et al.*, 2000; *Lyons et al.*, 2002; *Wdowinski*, 2009; *Jouanne et al.*, 2011; *Smith-Konter et al.*, 2011; *Weber et al.*, 2001].

In this work, we focus on the El Pilar Fault (EPF), a 350 km long strike-slip fault [e.g., *Soulas*, 1986; *Beltrán*, 1993, 1994; *Audemard et al.*, 2000] that extends eastward from the Cariaco Trough to the Gulf of Paria (Figure 1). The deformation associated with the active traces of the EPF has been identified by use of high-resolution offshore seismic reflection data [*Audemard et al.*, 2007; *Van Daele et al.*, 2011] and trenches [*Beltrán et al.*, 1996; *Audemard*, 2011]. Historical records date from the Spanish conquest in the early sixteenth century. Northeastern Venezuela experienced seismic events in 1530, 1684, 1766, 1797, 1853, and 1929 and on 9 July 1997, with the M_s 6.8 Cariaco earthquake along the strike-slip EPF [*Audemard*, 1999b, 2007]. Field reconnaissance of the ground breaks after the 1997 earthquake confirms that this event took place on the ENE-WSW trending onshore portion (~80 km) of the dextral EPF, between the gulfs of Cariaco and Paria, which is part of the major wrenching system within the Caribbean-South America plate boundary zone [*Audemard*, 2006]. The slip direction of this fault has been unequivocally confirmed by the dextral character of the surface break associated with the 1997 Cariaco earthquake [*Audemard*, 1997, 1999a, 2006] and by focal mechanism solutions for this event and its aftershocks [*Pérez*, 1998; *Baumbach et al.*, 1999, 2004; *Romero et al.*, 2002; *Audemard et al.*, 2005].

In this paper, we present results that include GNSS data from late 2003, late 2005, and the more recent early 2013 observation campaign and data from a cGNSS station called CUMA. This recent effort is intended to

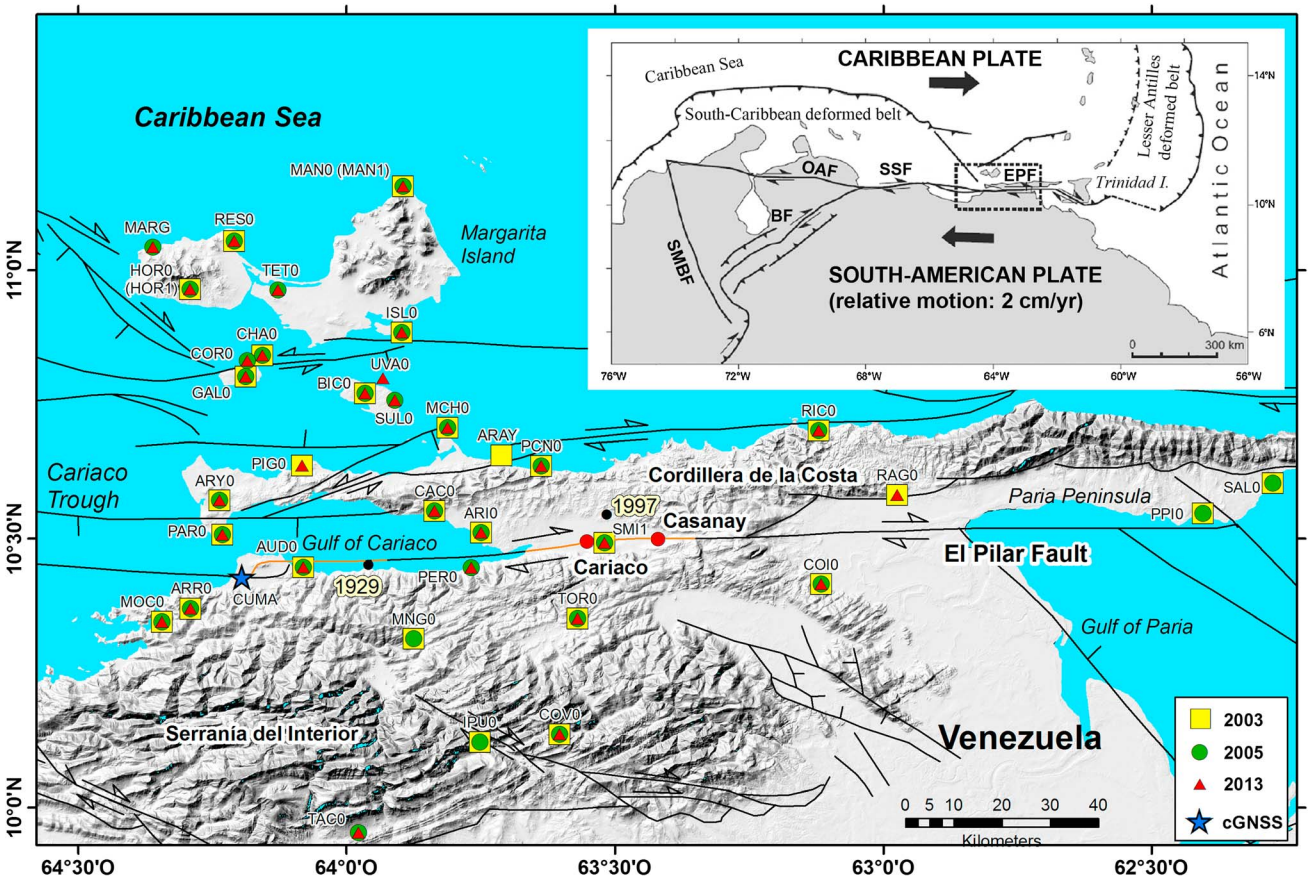

Figure 1. Location map of the active faults in northeastern Venezuela [*Audemard et al*., 2000] showing distribution of the GNSS stations: yellow squares, green circles, and red triangles are GNSS sites on which the acquisition campaigns were carried out in 2003, 2005, and 2013 respectively; the blue star corresponds to the cGNSS CUMA station of REMOS-IGVSB Network. We show the epicenter location of 1929 and 1997 events with their respective proposed ruptures (orange lines) [*Audemard*, 2007]. (top right) The inset box shows a schematic geodynamic map of the southeastern Caribbean [*Audemard*, 1999b; *Audemard et al*., 2000; *Weber et al*., 2001]. Legend: BF = Boconó Fault, EPF = El Pilar Fault, OAF = Oca Ancón Fault, SMBF = Santa Marta Bucaramanga Fault, and SSF = San Sebastian Fault.

constrain the velocity field along the EPF. We focus on the structure of the crust to better constrain seismic hazard through the evaluation of locking depth, far-field velocity, and aseismic slip.

This manuscript is structured as follows: In section 2, we describe GNSS data collection and processing. In section 3 and its subsections, we introduce several modeling approaches and develop the corresponding methodologies. This section includes the simple elastic half-space model, the asymmetric model, the compliant zone (CZ) model, the distributed-slip model, and the displacement-simulation method using nonvertical dislocations. In section 4, we compare the models using the Fisher-Snedecor test, and in section 5, we discuss several methods used in this paper and their significance for the study of the EPF.

2. Geological Setting

Northeastern Venezuela is part of the complex plate boundary zone of the Caribbean, South American, and Atlantic Plates. The Caribbean-South American plate boundary is described as a very wide active transpressional zone [*Soulas*, 1986; *Audemard*, 1993, 1998; *Beltrán*, 1994; *Singer and Audemard*, 1997] where plate motion is accommodated predominantly by the right-lateral strike-slip Boconó-San Sebastián-El Pilar-Los Bajos/El Soldado-Warm Springs fault system [*Molnar and Sykes*, 1969; *Minster and Jordan*, 1978; *Pérez and Aggarwal*, 1981; *Stephan*, 1982; *Aggarwal*, 1983; *Schubert*, 1984; *Soulas*, 1986; *Beltrán and Giraldo*, 1989; *Speed et al*., 1991; *Singer and Audemard*, 1997; *Pérez et al*., 2001a, 2001b; *Weber et al*., 2001; *Pindell and Kennan*, 2007; *Audemard*, 2009].

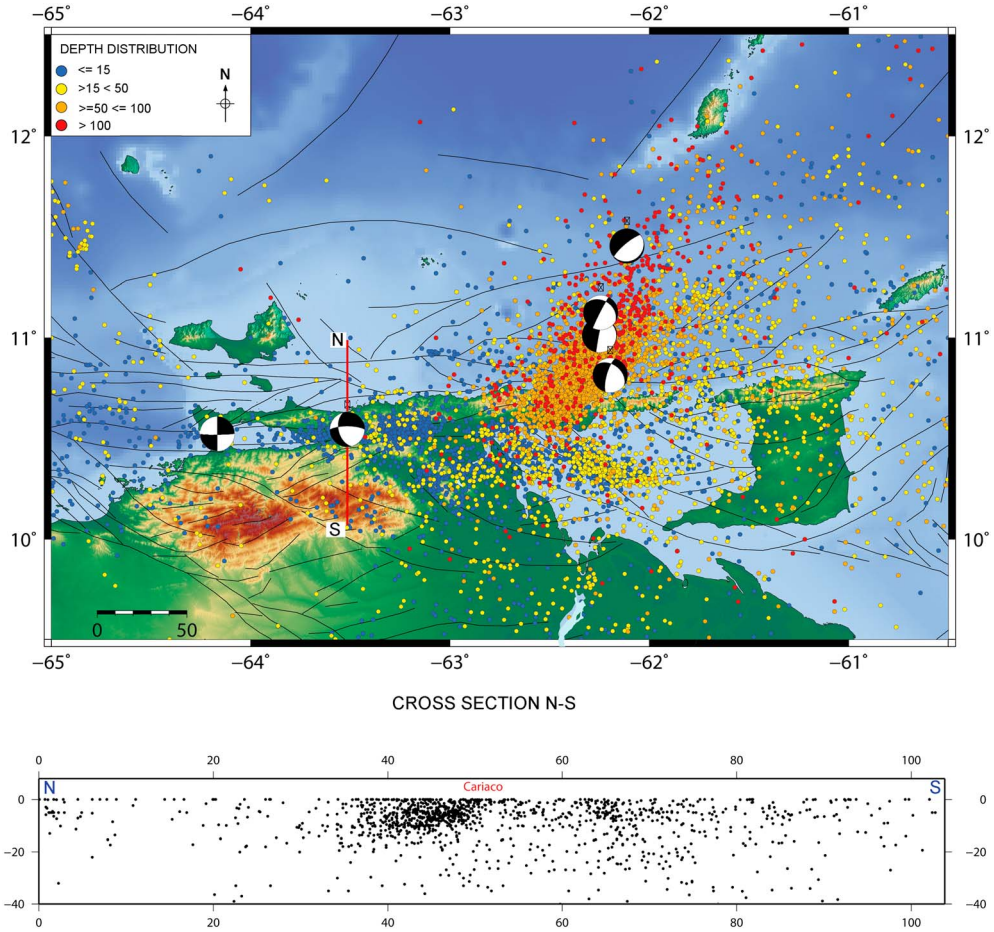

Figure 2. Distribution of seismicity in northeastern Venezuela from the 1910–2010 FUNVISIS catalog. The active faults are from *Beltrán* [1993] and focal mechanism from *Audemard et al*. [2005], and *Palma et al*. [2010].

The strike-slip EPF extends for some 350 km; however, its depth is not well constrained. *Vierbuchen* [1984] inferred from the steep gravity gradient across the EPF that the fault plane is a nearly vertical density discontinuity to a depth of at least 5 to 10 km. A depth of approximately 8 km was derived for the fault plane from seismic reflection profiles [*Schubert*, 1984] assuming an average *P* wave velocity of 5.2 km/s [*Baumbach et al*., 2004]. *Hernández et al*. [1987] suggested a depth of 15 to 20 km for the fault plane on the basis of a joint interpretation of seismic, magnetic, and gravimetric data.

More recently, other efforts have been made to constrain the EPF. Studies related to the 1997 Cariaco earthquake have limited the seismogenic portion of the EPF to the first 12 km at depth on the basis of the depth distribution of aftershocks [*Baumbach et al*., 2004]. *Clark et al*. [2008] on the basis of wide-angle onshore-offshore reflection/refraction modeling, ascertained a Moho depth of 48 km beneath the EPF. This depth corresponds to a depth increase of 16 km, coinciding with the dextral strike-slip system between the Coche Fault and the EPF. However, the region is mainly characterized by shallow intracontinental seismicity (in the first 20 km) associated with the EPF. Seismicity deeper than 40 km is related to the southern tip of the Lesser Antilles subduction zone under Trinidad and Tobago, the Paria Peninsula, and the active island arc of the Lesser Antilles (Figure 2).

The EPF roughly separates two very different geological provinces. On the northern side lies the Eastern Cordillera de la Costa, made up of Lower Cretaceous metasediments, metavolcanics, igneous rocks, and ophiolite remnants. These rocks have been metamorphosed into greenschist and blueschist facies and deformed by imbricated folds and thrust faults. On the southern side of the EPF, the Serranía del Interior exposes a fold-and-thrust belt, made up of nonmetamorphosed Cretaceous and Paleogene sediments

[*Metz*, 1965; *Vierbuchen*, 1984; *Jacome et al*., 1999]. A three-dimensional velocity tomography by *Grosser et al*. [2001] reveals that the material north of the EPF has a higher shear strength than the material south of the fault. *Baumbach et al*. [2004] point out that the aftershock distribution of the 1997 Cariaco earthquake had a very sharp boundary on the northern side of the EPF, contrasting with the more diffuse boundary on the southern side. From wide-angle seismic reflection/refraction, *Clark et al*. [2008] also report velocities decreasing southward to the EPF from 3.5 km/s to 2.2 km/s and a shallow region of relatively high velocities (>6.5 km/s), probably related to the exhumed metamorphic rocks of Margarita Island and the Araya-Paria Peninsula. Using a similar methodology, *Christeson et al*. [2008] present the results of a regional wide-angle seismic profile, indicating the transition from allochthonous terrane of fore-arc affinity to the passive margin of northern South America. The suture farther east between the Caribbean and South American Plates could be marked by the North Coast fault zone, transferring the present-day strike-slip motion between both plates some 30 km to the south.

3. Previous Studies

Deformation in northeastern Venezuela, based on geodetic measurements, has been recently described in several articles. *Pérez et al*. [2001a, 2001b] estimated the coseismic slip at depth responsible for the 1997 Cariaco earthquake by application of boundary element methods [*King and Nostro*, 1999] to derive surface-fault displacements [*Okada*, 1985]. The best solution corresponds to a fault plane segmented into three patches of 14 km ± 2 at depth and striking N84°E, with coseismic slips estimated at approximately 1 m. Current-derived velocities of the EPF by GNSS studies have been simulated in *Jouanne et al*. [2011] by the use of the Okada formulations [*Okada*, 1985] for an isotropic homogeneous half-space. Interseismic velocities simulated by *Jouanne et al*. [2011] indicate asymmetric velocity gradients on each side of the EPF as a result of dipping fault segments, as well as a lack of significant displacement (particularly shortening) in the Serranía del Interior on the southern side. That work demonstrated an eastward motion of up to 22 mm/yr (relative to the fixed South American Plate) of benchmarks on the northern side of the EPF and also the existence of substantial creep along the upper part of the EPF. Localized aseismic displacement along the fault has been revealed by the displacement of markers (roads, gutters, sidewalks, constructions, etc.) observed in the field in the years 1997–2003 after the 1997 earthquake [*Audemard*, 2006].

4. GNSS Data Collection and Analysis

To monitor and determine present-day displacements in northeastern Venezuela, a GNSS network was established in 2003 (Figure 1). Early in 2003, Venezuelan Foundation for Seismological Research (FUNVISIS) personnel installed 36 new brass benchmarks covering eastern Venezuela from the islands in the north to the stable Precambrian craton in the south (south of the Orinoco River). Four existing sites (one from Petroleos de Venezuela S.A. (PDVSA) and three from the University Navstar Consortium) were included to complete a set of 40 campaign stations. The Cumaná station (CUMA) belonging to the Red de Estaciones de Monitoreo Satelital GPS (REMOS, GPS Satellite Monitoring Station Network of Venezuela) from Instituto Geográfico Venezolano Simón Bolívar (IGVSB, Geographic Institute of Venezuela) was also included in this study. The GNSS network was measured in late 2003, late 2005, and early 2013 (Figure 3), providing data for 32 sites on at least two occasions. We used direct centering benchmarks with dual-frequency receiver and geodetic antennas, measuring at least two 24 h sessions for each site, while the AUD0 station was measured continuously throughout the campaigns. The available data from cGNSS CUMA (2008.5–2008.7, 2012.5–2013.5) was included.

Data from 33 stations (including the CUMA station) were analyzed by the application of Bernese 5.2 software [*Dach and Walser*, 2013], utilizing absolute antenna phase center offset models, together with the International GNSS Service (IGS) final precise orbits [*Beutler et al*., 1999], IGS Earth rotation parameters, and data from nearby permanent GNSS stations. We used the FES2004 ocean tidal model to calculate corrections for all GNSS stations using the Hans-Georg Scherneck web tool (http://www.oso.chalmers.se/~loading/). Velocities (Table 1) were estimated in the IGb08 frame of reference (an IGS-specific realization of ITRF2008) and expressed in the South America reference frame by the use of the ITRF2008 absolute plate rotation pole proposed by *Altamimi et al*. [2012]. We followed the resolution strategy with (1) initial ionosphere-free analysis with computation of residuals, (2) residuals analysis, (3) code-based widelane ambiguity resolution

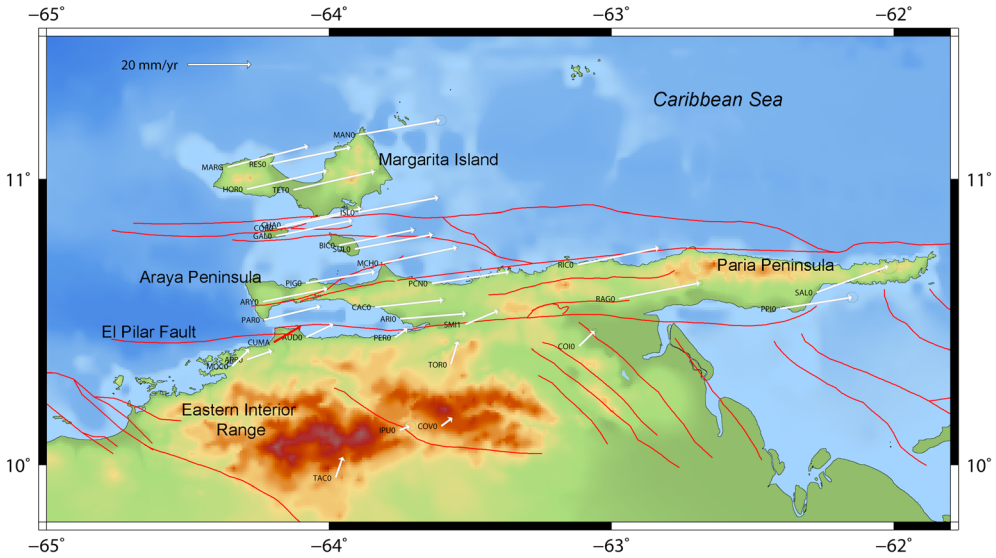

Figure 3. Observed velocities (white arrows) derived from comparison of 2003, 2005, and 2013 GNSS campaign measurements with error ellipses drawn for 66% confidence level [*Jouanne et al.*, 2011] and expressed within the South America Plate reference frame using the rotation pole proposed by *Altamimi et al.* [2012]. The red vector is the CUMA station (REMOS-IGVSB). The active faults in northeastern Venezuela are from *Audemard et al.* [2000]. Topography and bathymetry data are from *Lindquist et al.* [2004].

Table 1. Velocities Expressed in the IGb08 Reference Frame

Station	Longitude (deg)	Latitude (deg)	Ve (mm/yr)	Vn (mm/yr)	σVe (mm/yr)	σVn (mm/yr)
ARI0	−63.749	10.511	11.07	12.32	0.2	0.2
ARR0	−64.291	10.370	0.80	13.18	0.3	0.2
ARY0	−64.236	10.571	10.75	14.28	0.2	0.2
AUD0	−64.081	10.447	1.32	14.29	0.1	0.1
BIC0	−63.965	10.770	13.52	14.95	0.2	0.2
CAC0	−63.837	10.553	11.63	12.80	0.3	0.3
CHA0	−64.156	10.841	13.69	15.08	0.3	0.2
COI0	−63.116	10.415	−1.59	14.99	0.4	0.4
COR0	−64.184	10.831	13.88	15.10	0.3	0.2
COV0	−63.603	10.136	−2.74	13.16	0.2	0.2
CUMA	−64.195	10.429	13.69	14.90	0.1	0.1
GAL0	−64.188	10.802	14.61	15.62	0.2	0.2
HOR0	−64.291	10.965	−3.29	16.89	0.2	0.2
IPU0	−63.751	10.122	−2.91	12.00	1	0.9
ISL0	−63.896	10.884	14.66	14.72	0.2	0.2
MAN0	−63.895	11.156	14.99	14.61	1	0.9
MARG	−64.360	11.042	16.65	16.48	0.2	0.2
MCH0	−63.811	10.707	13.24	14.95	0.2	0.2
MOC0	−64.344	10.346	−1.27	15.26	0.2	0.2
PAR0	−64.231	10.508	8.67	14.36	0.2	0.2
PCN0	−63.637	10.636	14.03	13.94	0.2	0.2
PER0	−63.767	10.446	−2.42	13.30	0.4	0.3
PIG0	−64.083	10.637	11.86	13.81	0.3	0.2
PPI0	−62.404	10.547	12.67	14.02	1.0	0.9
RAG0	−62.974	10.582	15.00	15.10	0.4	0.4
RES0	−64.209	11.053	14.73	15.17	0.2	0.2
RIC0	−63.120	10.701	15.01	15.33	0.2	0.2
SAL0	−62.274	10.604	12.60	17.78	1.5	1.3
SMI1	−63.519	10.492	2.78	14.54	0.2	0.2
SUL0	−63.910	10.757	14.13	14.65	0.3	0.2
TAC0	−63.977	9.954	−3.75	16.30	0.3	0.3
TET0	−64.127	10.963	14.94	15.66	0.3	0.3
TOR0	−63.569	10.352	−3.82	16.88	0.2	0.2

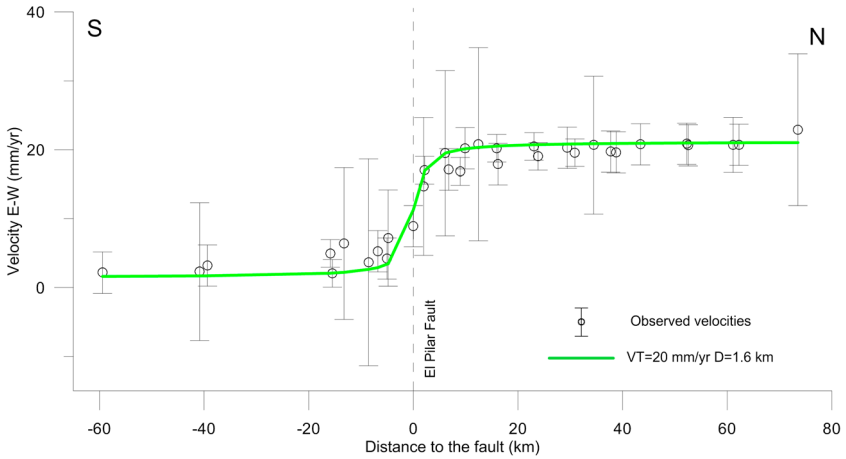

Figure 4. Velocity field across the EPF. Fault-perpendicular profile (solid line) showing the best fit model for the classic half-space dislocation model.

for all the baselines [*Melbourne*, 1985; *Wübbena*, 1985]; using differential code bias (DCB) files when available and computation of the ionosphere-free solution with the introduction of the resolved Melbourne-Wübbena linear combination ambiguities, (4) phase-based widelane (L5) ambiguity resolution for baselines < 200 km and computation of the ionosphere-free solution with the introduction of resolved ambiguities, (5) resolution of the previously unresolved ambiguities for baselines < 2000 km using the quasi ionosphere-free strategy of resolution, (6) direct L1/L2 ambiguity resolution for baselines < 20 km, and (7) computation of the normal equations. The daily GNSS solutions were transformed in the IGb08 reference frame [*Altamimi et al.*, 2012] with a six-parameter Helmert solution (three translation parameters and three rotation parameters) using the IGS stations BOGT, BRAZ, BRFT, BRMU, CIC1, CRO1, FORT, GLPS, GMAS, GUAT, MANA, MAS1, MDO1, SANT, SCUB, and SSIA. We detected outliers with the Find Outliers and Discontinuities in Time Series tool in the Bernese software that reduces, step by step, the discrepancy between the functional model and the time series from statistical adjustment [*Ostini et al.*, 2008]. The Bernese software underestimates the daily coordinate errors because systematic errors or mismodeled parameters are not included in the formal error [*Hugentobler et al.*, 2001]. To obtain a realistic estimated error, we rescaled the formal errors multiplying by a factor of 10.

5. Modeling Approaches

The velocity field across the EPF zone exhibits two separate patterns. Sites south of the EPF show smaller displacements than those north of the fault (Figures 3 and 4). The IPU0 site velocity with respect to South America does not exceed 3 mm/yr. Similarly, velocities at other sites range from ~4 mm/yr (COV0) to ~8 mm/yr near to the fault segment. The SMI1 site close to the rupture zone of the 1997 Cariaco earthquake presents a velocity of ~9 mm/yr. By contrast, immediately upon crossing the EPF, the ARI0, and PAR0 sites exhibit velocities of ~15 mm/yr. This pattern continues to Margarita Island, where a velocity of ~21 mm/yr is observed at the MAN0 site. A few kilometers on either side of the EPF, a high-displacement gradient crossing the fault suggests a shallow locking depth or an aseismic component along the upper part of the EPF. As mentioned above, the asymmetric displacement gradients on each side of the EPF have been associated with dipping fault segments [*Jouanne et al.*, 2011].

A first-order model of interseismic deformation [*Chinnery*, 1961; *Weertman and Weertman*, 1964; *Savage and Burford*, 1973] (equation (1)) is given by

$$v(x) = \frac{V_T}{\pi} \tan^{-1}\left(\frac{x}{D}\right), \tag{1}$$

where $v(x)$ is the velocity at a distance x from the fault, V_T is the far-field velocity, and D is the locking depth of the fault. Our results show a 1.6 km locking depth and a far-field velocity of 20 mm/yr, according to the most widely accepted Caribbean-South American Plate motion values [*DeMets et al.*, 2000; *Pérez et al.*, 2001a, 2001b; *Weber et al.*, 2001].

Although the fault-perpendicular profile based on the homogeneous elastic half-space model shows a relatively good fit (Figure 4), we propose to model this velocity field using four approaches that include other considerations: (1) the possibility of explaining the asymmetric velocity gradients by contrasting material properties on each side of a vertical fault, (2) the presence of a compliance zone (a near-fault low-rigidity tabular zone) on either side of the fault caused by cumulative damage from repeated earthquakes, (3) a distributed-slip estimation through utilization of multiple finite discrete fault patches to simulate a gradual transition of slip rates rather than a sudden jump, and (4) an upgrade by the use of 2013 data of the displacement simulation method described in *Jouanne et al*. [2011] by application of nonvertical dislocations to simulate the deeper parts of the EPF.

5.1. Change in Elastic Properties on Each Side of the EPF

Here we explore the asymmetry of elastic properties on each side of the EPF. We consider a single vertical fault separating two geologic terrains with contrasting Young's moduli. We use the half-space model modification [*Jolivet et al*., 2009] to the asymmetric dislocation model proposed by *Le Pichon et al*. [2005] to calculate an asymmetric surface velocity field on each side of the vertical fault located at $x = 0$ (equations (2) and (3)). We consider three parameters: the rigidity contrast between the two sides of the fault, the horizontal offset between the fault zone at depth and its surface trace, and the fault slip rate:

$$v(x) = \frac{2KV_T}{\pi} \tan^{-1}\left(\frac{x}{D}\right); x < 0, \tag{2}$$

$$v(x) = 2(1-K)\frac{V_T}{\pi} \tan^{-1}\left(\frac{x}{D}\right); x \geq 0, \tag{3}$$

where, again, $v(x)$ is the velocity at a distance x from the fault, V_T is the far-field velocity, and D is the locking depth of the fault. The asymmetry coefficient $K = V1/(V1 + V2)$; $K = V1/V_T$ ranges from 0 to 1 and can also be expressed as $E_2/(E_1 + E_2)$, E_1 and E_2 being the Young's moduli on both sides of the EPF. Equations (2) and (3) are equivalent to $K = 0.5$, meaning there is no rigidity contrast. To evaluate the quality of our models, we calculate an RMS or the quadratic mean value of the misfit (equation (4)) as follows:

$$\mathrm{RMS} = \sqrt{\frac{1}{N}\sum\left(\frac{(\mathrm{Ve_{obs}} - \mathrm{Ve_{model}})^2}{\sigma^2_{\mathrm{Veobs}}}\right)}, \tag{4}$$

where $\sigma^2_{\mathrm{Veobs}}$ is the variance of the observations, $\mathrm{Ve_{obs}}$ is the eastern component velocity from interseismic velocities of the northeast Venezuelan GNSS network, $\mathrm{Ve_{model}}$ is the simulated velocity, and N is the number of GNSS stations along the EPF.

The best fit for an unconstrained model suggests a far-field velocity of 17 mm/yr, with a 1.5 km locking depth and an asymmetry ratio of 0.33. To enhance the robustness of our results, we evaluate trade-offs between the rigidity ratio and locking depth, rigidity ratio and slip rate, and locking depth versus slip rate (Figures 5a–5c) for this model. We determine that the rigidity contrast is almost constant, whereas the locking depth can vary between 1.5 and ~5 km, and the fault slip rate can vary between ~15 and 18.5 mm/yr. Nonetheless, there is a significant trade-off between locking depth and slip rate, with deeper locking depth leading to higher far-field velocities.

Likewise, we evaluate two possibilities, starting from the following two sets of conditions: (1) a far-field velocity constrained to 20 mm/yr similar to the classic half-space dislocation model and (2) a second test fixing the locking depth at 12 km, according to the distribution versus depth of microseismicity [*Baumbach et al*., 2004]. The best fit for the first model is a 3.0 km locking depth with a K ratio of 0.37. For the second model, the best fit is a 24 mm/yr far-field velocity and an asymmetry ratio of 0.36. For both models, trade-off between the rigidity ratio versus locking depth and slip rate, respectively, reveals no significant variation in rigidity contrast, with decreasing or increasing locking depth and slip rate (Figures 5d and 5e). Fault-perpendicular velocity profiles show a good fit for all models (Figure 6a). The observed velocities with their eastern component from GNSS campaigns and unconstrained model simulated velocities are shown in Figure 6b.

5.2. Compliant Fault Zone Model

Crustal faulting can often be associated with the development of highly fractured and damaged rocks around the main slip surface. The cumulative damage caused by repeated earthquakes might generate a weaker

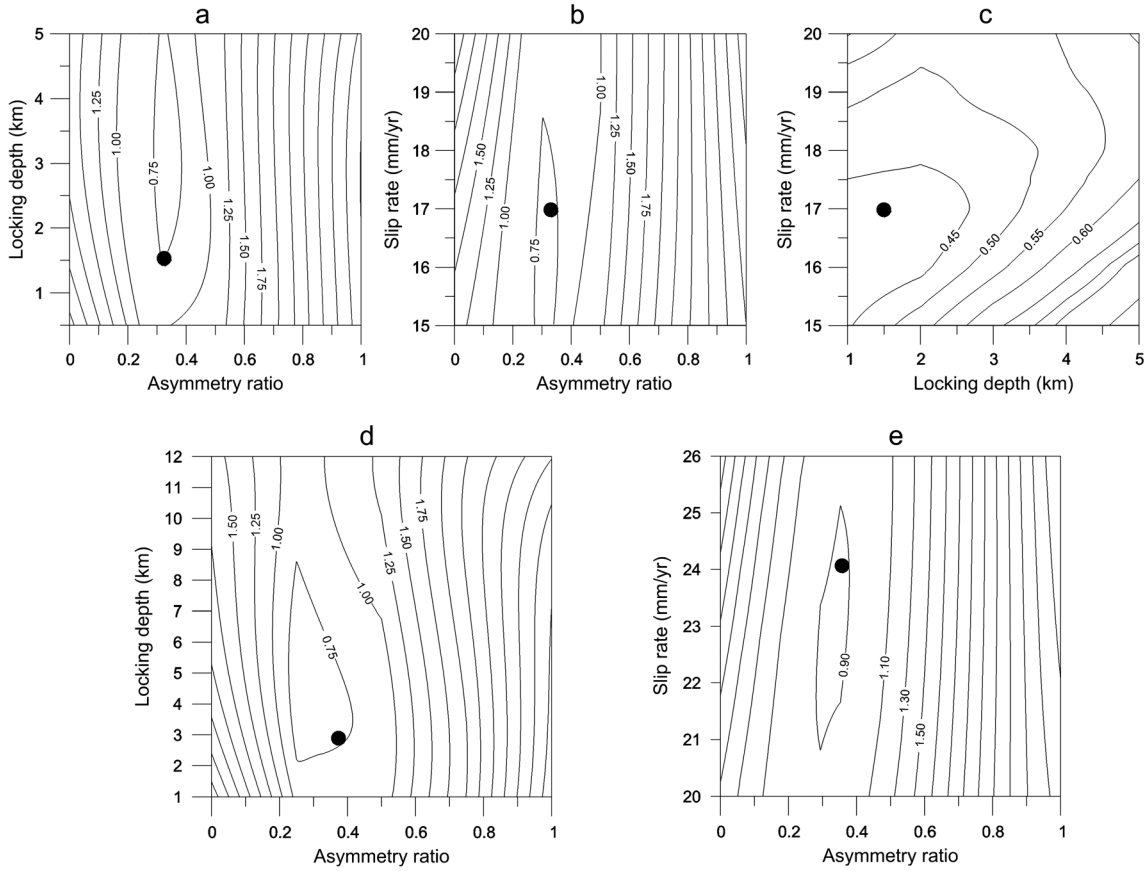

Figure 5. Trade-offs between (a) asymmetry ratio and locking depth, (b) asymmetry ratio and slip rate, and (c) locking depth versus slip rate for the unconstrained model (Results. $V_T = 17$ mm/yr, $D = 1.5$ km, and $K = 0.33$). (d) Trade-off between the asymmetry ratio and the locking depth on the EPF for the model with far-field velocity fixed at 20 mm/yr. (e) Trade-off between the asymmetry ratio and the slip rate on the EPF for the model with locking depth fixed at 12 km. Contoured values are the RMS values and the black dot indicates the best model.

zone than the surrounding medium [*Ambraseys*, 1970; *Wilson et al*., 2005; *Chester et al*., 2005, *Peng and Ben-Zion*, 2006]. We investigate the influence of a CZ around the EPF using a semianalytic iterative procedure based on a three-dimensional model of elastostatic deformation in a semi-infinite solid, with a free-surface boundary condition and three-dimensional variation in elastic properties [*Barbot et al*., 2009]. This method, adapted to the case of three-dimensional deformation, is based on a numerical approach presented by *Barbot et al*. [2008]. This procedure simulates the deformation caused by faulting in the presence of arbitrary variations in material properties that are modeled with equivalent body forces and equivalent surface traction in a "homogenized" elastic medium. The surface displacement is obtained in the Fourier domain by application of a semianalytic Green function. In this work, we explore models that include a CZ that is shallower than the locking depth [*Jolivet et al*., 2009] extending downward from the surface and following the strike of the EPF. *González et al*. [2004] report that damage from the 1997 Cariaco earthquake is most pronounced along the EPF because of a strong anisotropy or directivity effect caused by fault orientation and rupture propagation as well as the general W-E alignment of the regional structure.

The input model parameters include the gradient of Lamé parameters $\Delta\lambda$ and ΔG, the CZ width (fault-normal dimension), and depth (downdip dimension), together with EPF geometry. We constrain several parameters such as strike, dip, and rake directions for the EPF on the basis of earlier work [e.g., *Audemard et al*., 2000; *Mendoza*, 2000; *Pérez et al*., 2001a, 2001b; *Baumbach et al*., 2004; *Jouanne et al*., 2011]. The asymmetric velocity gradient on either side of the EPF is considered an important feature to fit the data. We have controlled this parameter by introducing dipping fault segments [*Jouanne et al*., 2011]. The transition between the upper seismogenic and lower ductile dislocations was fixed at 12 km on the strength of the aftershock depth distribution of the 1997 Cariaco earthquake [*Baumbach et al*., 2004].

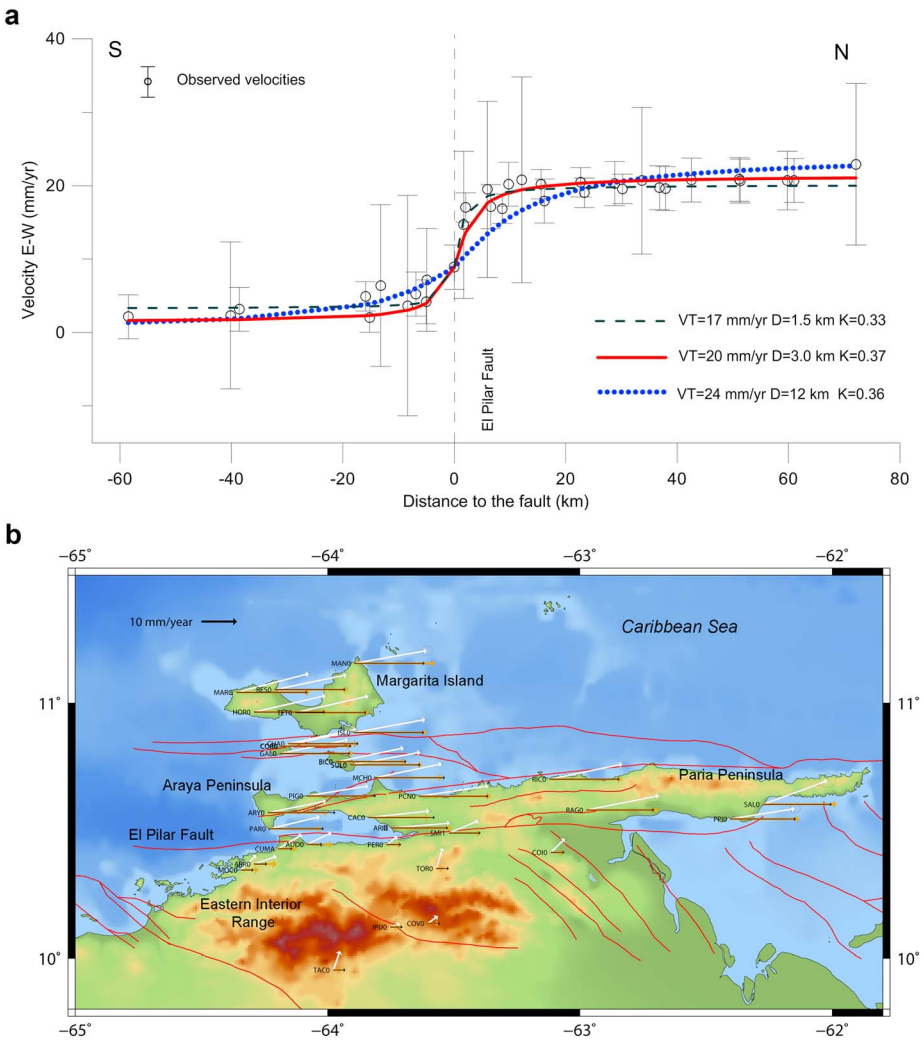

Figure 6. (a) Fault-parallel velocity profiles showing the acceptable models from the asymmetric modeling in the EPF zone and the E-W observed velocities from 2003, 2005, and 2013 GNSS campaign measurement data (including cGNSS CUMA station). (b) Observed velocities (white arrows) with their eastern component (yellow arrows) from GNSS campaigns and simulated velocities (black arrows) from the unconstrained parameters asymmetric model. All displacements are based on the South America reference frame.

First, to identify the best fitting model, we explore a range of different widths and depths for the CZ, ranging from 0 to 3 km and 0 to 12 km, respectively, according to the $W = L/6$ ratio presented by *Barbot et al.* [2008] who assumed that the CZ width is 6 times smaller than the depth extent of the coseismic slip, where L is the nominal locking depth. Nonetheless, we extend the range of CZ width (to 12 km) in line with *Cochran et al.* [2009] who report that width differences of damaged zones may be related to intrinsic variations along sections of the same fault. In addition, we evaluate the rigidity reduction, ranging from −30% to −60% (we assume the same values for the ΔG and $\Delta\lambda$ parameters for each calculation) relative to the surrounding lithosphere.

We evaluate the quality of our models with an RMS of the misfit on the basis of comparison between simulated and observed interseismic velocities of the northeast Venezuelan GNSS network (equation (5)), as follows:

$$\mathrm{RMS} = \sqrt{\frac{1}{N}\left(\sum \frac{(\mathrm{Ve}_{\mathrm{obs}} - \mathrm{Ve}_{\mathrm{model}})^2}{\sigma^2_{\mathrm{Ve}_{\mathrm{obs}}}} + \sum \frac{(\mathrm{Vn}_{\mathrm{obs}} - \mathrm{Vn}_{\mathrm{model}})^2}{\sigma^2_{\mathrm{Vn}_{\mathrm{obs}}}}\right)}. \quad (5)$$

To improve our evaluation, we test several possibilities, considering EPF as a one-to-four-segment fault (two, four, six, and even eight dislocations, respectively). However, the best models according to the number of segments (from one to four segments) show a good adjustment between observed and simulated

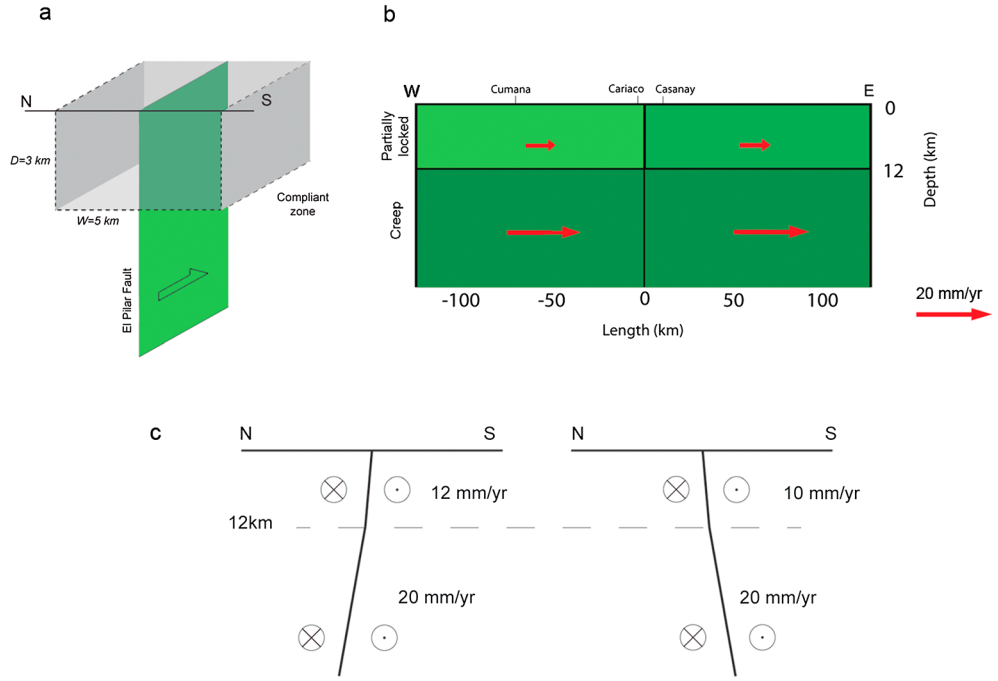

Figure 7. (a) Diagram of a CZ within the upper 3 km in depth and a 5 km width surrounding and following the strike of the EPF. (b) Distribution of right-lateral slip on the northern side of the EPF and (c) cross sections of western and eastern segments of the EPF according to two-segment CZ dislocation model. The western and eastern segments are shown with a northward and southward dipping fault, respectively, and substantial aseismic slip along the upper part of the fault.

velocities, with similar responses to the CZ parameter variations. Our preferred models, independent of the number of EPF segments, indicate a CZ within the upper 3 km depth and 1–5 km wide, with a slight improvement by application of a rigidity reduction of $\Delta G = -30\%$ (Figures 7a and 8).

Nevertheless, to evaluate the improvement in the models according to the number of fault segments, we compare the best solutions for each number of segments using the Fisher-Snedecor variance test. This evaluation, based on different degrees of freedom and RMS values, is used to estimate the probability of differences between two comparable models (Table 2). To perform this test, we consider the strike-slip displacement component only for the interseismic slip, ruling out the dip-slip contribution for the EPF (the vertical displacement has not been evaluated in this work) in accordance with *Audemard* [2006] who, using a set of geological and structural observations gathered along the surface rupture of the Cariaco 1997 earthquake, has indicated that the overall direction of motion on the EPF is right-lateral with no visible vertical component. Results show that the "CZM 4 dislocations: two segments" model with its range of 58% to 87% is probably better than the others. The trade-off between CZ depth and width reveals a reduction in adjustment with an increase in these parameters. The differences for several rigidity reduction values are almost imperceptible. For this reason, we do not show the respective contour plots.

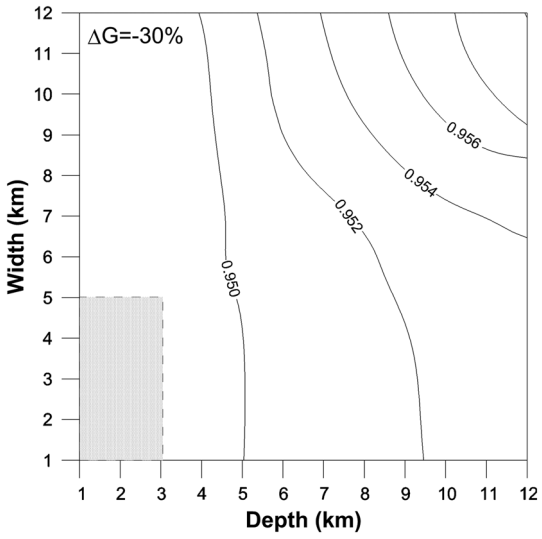

Figure 8. Trade-off between depth and width CZ for a rigidity reduction ΔG of 30%. Contoured values are the RMS values, and the rectangular zone indicates the preferred models.

The EPF geometry for this preferred model shows in the upper segments an 85° northward dip for

Table 2. Selection of Best Compliant Zone Model (CZM) According to Fisher-Snedecor Variance Test

Model	*N* Data	*N* Parameters	Degree of Freedom	RMS
CZM 2 dislocations (one segment)	66	11	55	1.291
CZM 4 dislocations (two segments)	66	15	51	1.144
CZM 6 dislocations (three segments)	66	23	43	1.228
CZM 8 dislocations (four segments)	66	27	39	1.211
Comparison of Models		**Test**	**Probability**	**Results**
Is the CZM 4 model better than the CZM 8 model?		1.384	0.86	Yes
Is the CZM 4 model better than the CZM 6 model?		1.273	0.80	Yes
Is the CZM 4 model better than model the CZM 2 model?		1.046	0.56	Maybes

the western segment and an 85° southward dip for the eastern segment, with 12 mm/yr and 10 mm/yr of displacement, respectively. The dextral strike-slip component along the deeper dislocations was constrained at 20 mm/yr to represent the ductile creep at depth. Dip was fixed with an 80° northward dip for the western segment and an 80° southward dip for the eastern segment (Table 3 and Figures 7b and 7c). From the comparison of upper displacement values with the 20 mm/yr relative velocity motion between the Caribbean and South American Plates, we find 40% of the locked displacement (20–12 = 8 mm/yr, 40% locked) in the western segment and 50% of locked displacement in the eastern segment (20–10 = 10 mm/yr, 50% locked), which is consistent with the observation of creep at the surface along the fault [*Audemard*, 2006] and the model proposed by *Jouanne et al*. [2011]. In Figure 9, we show the comparison between observed and simulated velocities for a two-segment CZ model.

5.3. Distributed-Slip Model From GNSS Observations

Based on the fact that friction along the fault plane is not uniform in intensity, the fault slip distribution can be evaluated in multiple finite discrete fault patches to detect variations in slip along the fault. The presence of stuck or locked zones, partially locked zones, and creeping zones is evaluated from interseismic displacements by the use of a procedure based on the constrained least squares method [*Wang et al*., 2013]. This method of slip inversion is performed by application of SDM2011 software, which has recently been applied in other geodetic studies [*Motagh et al*., 2008, 2010; *Wang et al*., 2009, 2011; *Xu et al*., 2010; *Diao et al*., 2010, 2011]. The observed slip data are related to the discrete fault displacement using a Green function of the Earth model calculated through the linear elastic dislocation theory. The ill-posed inverse problem is regularized by enforcing smoothness of solution by the use of Laplacian damping. The objective function is defined as follows:

$$F(\mathrm{b}) = \|\mathrm{Gb} - \mathrm{y}\|^2 + \alpha^2 \|\mathrm{H}\tau\|^2, \tag{6}$$

where G is the Green function, b is the slip of subfaults, y indicates the ground observation, τ is the shear stress drop related to the slip distribution on the whole fault plane, H represents the finite difference approximation of the Laplacian operator multiplied by a weighting factor proportional to the slip amplitude, and α^2 is the positive smoothing factor.

To invert the velocity field, we use the observed displacement data related to the discrete fault slips utilizing a homogeneous Earth model with a Poisson ratio of 0.25. We constrain the input geometry of the EPF to a western segment of ~96 km and an eastern segment of ~144 km, but we test several dip values as follows: (a) a geometry similar to the preferred CZ model (discussed above) with a northward dip for the western segment and southward dip for the eastern segment, respectively, 85° and 80°, for the upper and lower segments; (b) a geometry with the previous dips for the shallower segments but with a vertical segment

Table 3. Summary of Fault Geometry Input Parameters for Better Models

		Upper Segments			Lower Segments		
		Azimuth	Dip	Slip	Azimuth	Dip	Slip
Compliant zone model and	Western	90°	85° northward	12 mm/yr	90°	80° northward	20 mm/yr
Distributed slip (model a)	Eastern	90°	85° southward	10 mm/yr	90°	80° southward	20 mm/yr
Displacement simulation	Western	88°	87° northward	12 mm/yr	88°	53° northward	20 mm/yr
Jouanne et al. [2011]	Eastern	89°	77° southward	10 mm/yr	89°	80° southward	20 mm/yr

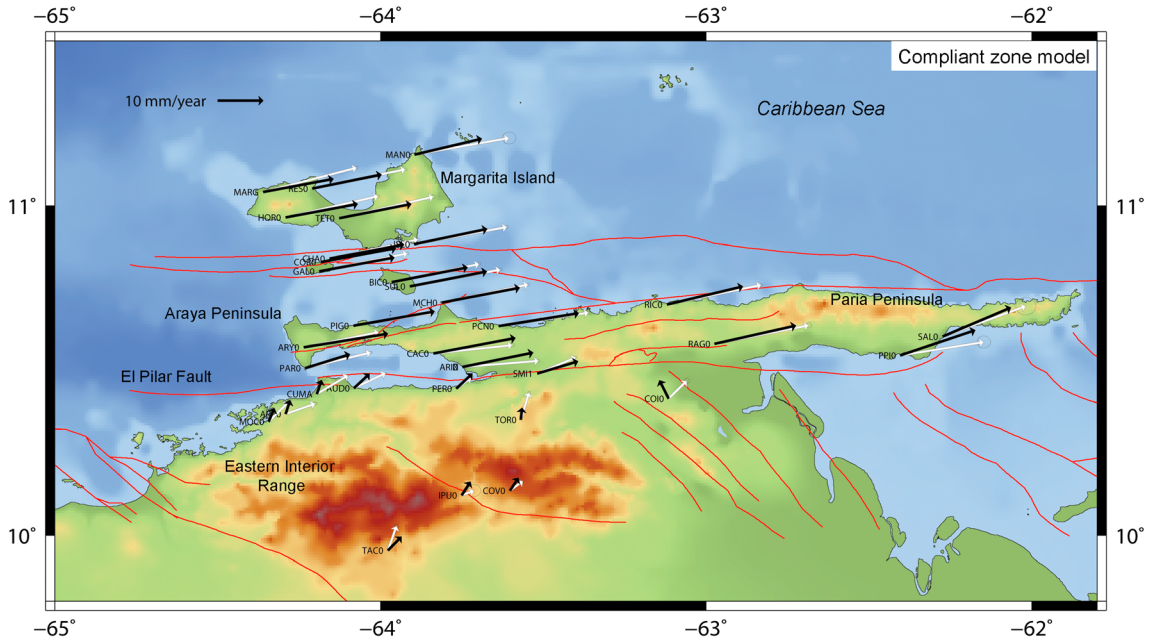

Figure 9. Observed velocities (white arrows) with error ellipses for 66% confidence level and simulated velocities (black arrows) according to the two-segment CZ modeling. All displacements are based on the South America reference frame.

below 12 km; and (c) a geometry for which all segments are considered to be vertical faults (Figures 10a–10c). In all cases, the upper segments are discretized into an array of ~2 km by 2 km patches and the lower parts are discretized into ~20 km by 20 km patches, with 90° strike and −180° rake values. Patch size is selected according to the length of subfaults used in previous studies and the maximum number of point sources permitted by the code. The larger patches were used for the lower parts to constraint the far-field velocity to a few iterations. We extend the area limits considerably to avoid any artificial boundary effect.

The fit to the data for all models is quite good, with ~95%–97% by the use of a standard linear least squares minimization when the interseismic velocities are compared with the simulated velocities. All segments are characterized by significant creep. Nevertheless, the upper western segment exhibits a significant decline in slip close to Cumaná City and in a minor area south of the CAC0 site, and the remainder of the segment exhibits a widespread partial creep pattern with creep larger than 12 mm/yr. In the upper eastern segment, we observe a zone (10–12 km in depth) with decreasing slip values, possibly related to the discontinuity effect at 12 km dislocation. We avoid this effect by considering all segments with a similar dip (Figure 10c). The contact between western and eastern upper segments displays a similar pattern near the city of Cariaco. If we dismiss these effects, the eastern upper segments exhibit widespread partial creep of ~8–12 mm/yr. Figure 11 shows the comparison between observed and simulated velocities for the vertical fault model.

5.4. Displacement Simulation Method Using Nonvertical Dislocations

Here we propose an upgrade of the model presented by *Jouanne et al.* [2011] including the 2013 data to supplement data from the 2003 and 2005 campaigns. To simulate the velocity field, we present a set of dislocations in a uniform elastic half-space for rectangular sources [*Okada*, 1985]. The inversion procedure is based on iterative least squares adjustments of free parameters such as dip, azimuth, dip slip, strike slip, and rake.

For this study, we increase the number of GNSS stations from the 23 stations simulated by *Jouanne et al.* [2011] to 33 stations (Figure 12). Nonetheless, we keep two segments (western and eastern) representing the EPF with upper and lower dislocation separations at 12 km, in line with the depth distribution of the 1997 event. We consider as free parameters the dip of the deeper dislocation dip and the slip rates along both parts (upper and lower) of the EPF, whereas the location, orientations, and upper dislocation dip are considered to be fixed parameters. Similar to the results of *Jouanne et al.* [2011], our preferred model shows

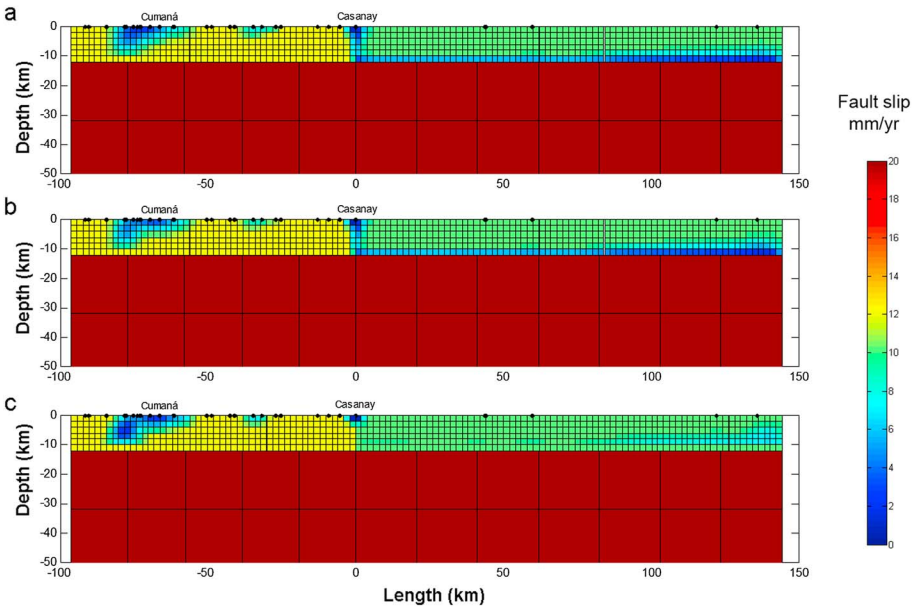

Figure 10. Distribution of right-lateral slip (mm/yr) on the EPF from distributed-slip modeling for (a) an input geometry similar to the preferred CZ model (Figure 7c). (b) Lower segment dip (>12 km depth) fixed to 90° and (c) upper and lower segments fixed to 90°.

the western segment to have an almost vertical upper segment and a 53° northward dipping deep segment. The eastern segment is characterized by a 77° southward dipping upper segment and an 80° southward dipping lower segment (Table 3) [see *Jouanne et al.*, 2011]. Likewise, the 12 mm/yr and 10 mm/yr of interseismic displacements are calculated for the western and eastern upper segments, respectively, and the dextral strike-slip component along the lower dislocations is fixed at 20 mm/yr.

6. Comparison of the Various Models

To discuss the best solution from models analyzed in this paper, we plot the E-W velocities versus the distance to the fault and residuals for different models (Figures 13a and 13b). A better fit of the unconstrained

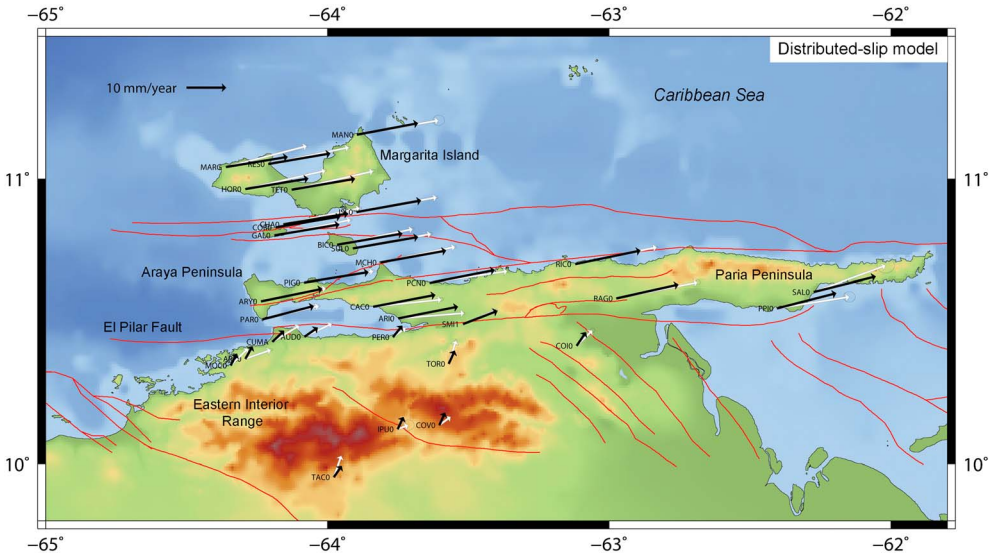

Figure 11. Observed velocities (white arrows) with error ellipses for 66% confidence level and simulated velocities (black arrows) according to the distributed-slip model for the vertical fault geometry (Figure 10c). All displacements are based on the South America reference frame.

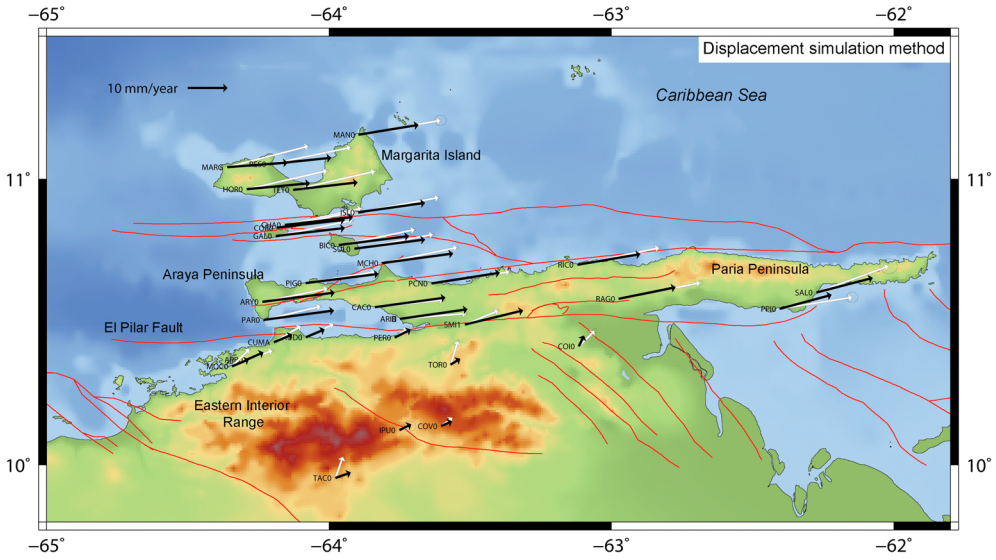

Figure 12. Observed velocities (white arrows) with error ellipses for 66% confidence level and simulated velocities (black arrows) according to the upgrade of displacement-simulation method. All displacements are based on the South America reference frame.

asymmetry model and the simplest half-space elastic model can be observed mainly on the north side of the EPF with respect to other inversions. Nevertheless, for the south side of the EPF, a best model is difficult to identify at first sight. For this reason, we apply a Fisher-Snedecor variance test to compare our best results from the homogeneous model, asymmetric model, near-fault reduced rigidity zone model, and

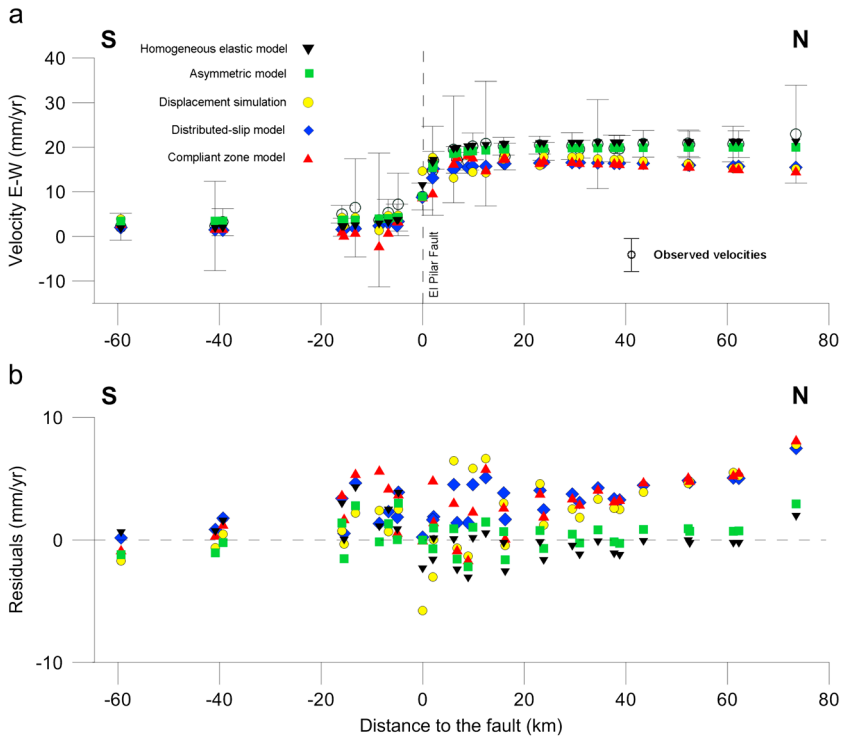

Figure 13. (a) Velocity field across EPF for several models applied in this work. We show E-W observed velocities and simulated velocities from the classic half-space dislocation model, the unconstrained asymmetric model, the displacement-simulation method, the distributed-slip model, and the two segment compliant zone model. (b) Residuals for the different models.

Table 4. Comparison of the Various Models According to Fisher-Snedecor Variance Test

Model	*N* Data	*N* Parameters	Degree of Freedom	RMS
Homogeneous model	33	2	31	0.542
Asymmetric model	33	3	30	0.375
CZM 4 dislocations (two segments)	66	15	51	1.144
Displacement simulations	66	20	46	1.242

Comparison of Models	Test	Probability	Results
Is the asymmetric model better than the homogeneous model?	1.399	0.82	Yes
Is the homogeneous model better than the CZM 4 model?	1.283	0.77	Yes
Is the asymmetric model better than the CZM 4 model? I	1.794	99.96	Yes
Is the CZM 4 model better than the displacement simulations model?	1.204	0.74	Yes

displacement-simulation method using nonvertical dislocations. We omit the distributed-slip model from this comparison because the discretization of segments into patches generates a much lower degree of freedom, making it incomparable with the other models.

We select our preferred result for each category of model (Table 4). Using the Fisher-Snedecor test of variances, we determine the probability of one model being better than another. The asymmetric model is most likely the best model, with 82% probability of being better than the homogeneous model. Likewise, the homogeneous model is shown to be a better model than the CZ model, and this last model is probably a better model, with more than 70% probability, with respect to the displacement simulation models. This outcome indicates that the asymmetric model is the best model from the statistical point of view. However, the existence of progressively displaced markers suggests the occurrence of substantial creep, and this aspect is not included in the asymmetric model.

7. Discussion

In this paper, we have applied five different methods of analyzing the velocity field across the EPF. From observation of parallel-fault velocities and the Fisher-Snedecor variance test, we have identified the asymmetric model as the best model. Nonetheless, each inversion test shows an interesting approach that we discuss in the following subsections.

7.1. Change in Elastic Properties on Each Side of the Fault

Asymmetric interseismic strain, recognized in major faults around the world (e.g., North Anatolian Fault, San Andreas Fault, and Great Sumatra Fault), has been explained by lateral variations in the depth of the brittle-ductile layer [*Schmalzle et al.*, 2006; *Chéry*, 2008; *Fulton et al.*, 2010], lateral variations in viscosity [*Malservisi et al.*, 2001], and the juxtaposition of materials with different physical properties [*Le Pichon et al.*, 2005; *Jolivet et al.*, 2008, 2009; *Houlié and Romanowicz*, 2011]. We have tested the hypothesis that asymmetric elastic properties may explain the observed velocity field on both sides of the EPF. From the results of this work, we show that the heterogeneous model, assuming a single vertical fault separating two blocks with different elastic properties, can provide a possible answer to the asymmetry of displacement gradients, and it can be an alternative to the assumption of dipping fault segments presented by *Jouanne et al.* [2011]. In this study, we evaluate this explanation for the asymmetric velocity field, taking into account the fact that the discontinuously changing elastic effect across the fault produces an asymmetry that can be quantified. We evaluate this model on the basis of the idea that the EPF roughly separates two very different geologic provinces. The different tests applied to the EPF point out a contrast of rigidity between the northern and southern sides of the EPF. The K ratio values of 0.33, 0.37, and 0.36 (Figure 6a) show that the igneous-metamorphic northern side has a rigidity of 2.0, 1.7, and 1.8 times, respectively, higher than the southern sedimentary side. Therefore, the idea of geologic property differences on each side of the EPF helps explain the asymmetric velocity field.

The marked displacement gradient across a few kilometers on either side of the fault suggests the possibility of a shallow locking depth or an aseismic component along the upper part of the fault plane [*Jouanne et al.*, 2011]. As results from the asymmetric model, we find a 1.5 km locking depth for the unconstrained asymmetric model. The locking depth value is significantly shallower than the seismogenic depth of 12 km. However, geodetic

locking depths that are shallower than the seismogenic depths have also been observed along the creeping segment of the San Andreas Fault [*Smith-Konter et al*., 2011] and the San Jacinto fault zone [*Wdowinski*, 2009]. Moreover, closer to the EPF, *Weber et al*. [2011] discuss a similar behavior on the Caribbean-South America plate boundary, specifically in the Central Range Fault of Trinidad and Tobago, obtaining a best fit single-fault elastic dislocation model with a 1–2 km locking depth and 12 ± 3 mm/yr of dextral strike slip, suggesting essentially fault creep across that fault. The shallow locking depth indicates that steady motion along the fault also occurs within the seismogenic crust of the EPF (0–12 km depth), in accordance with the idea that a significant slip associated with creeping or partially creeping fault segments can also occur within the seismogenic crust, and it is related to seismic or microseismic activity. Although eastern Venezuela is the most seismically active area on the southern Caribbean plate boundary, as documented by the FUNVISIS 1910-to-date instrumental seismicity catalog, most of the earthquakes are of magnitude 2–3. The main part of the Cariaco earthquake aftershocks (~80%), with magnitudes between −0.5 and 4.1, occurred in the depth range of 4.5 to 12 km [*Baumbach et al*., 2004], below the shallow locking depth obtained in this present study. The discrepancies between the maximum seismicity depths and the geodetic locking depth could be related to the possibility of shallow creep or temporary variations in strain release throughout the earthquake cycle [*Smith-Konter et al*., 2011].

7.2. Compliant Zone Modeling

As a consequence of crustal faulting, CZs have been observed around major faults (e.g., San Andreas Fault and North Anatolian Fault). The damage fault zones have been observed geologically in the field [e.g., *Chester and Chester*, 1998; *Ben-Zion and Sammis*, 2003; *Faulkner et al*., 2003; *Oskin and Iriondo*, 2004; *Dor et al*., 2006]. In addition, theoretical models [e.g., *Kachanov*, 1986; *Lyakhovsky et al*., 2001; *Turcotte et al*., 2003] and geodetic [e.g., *Chen and Freymueller*, 2002; *Fialko et al*., 2002; *Fialko*, 2004; *Hamiel and Fialko*, 2007; *Barbot et al*., 2009] and seismic observations [e.g., *Li et al*., 1994; *Ben-Zion et al*., 2003; *Thurber et al*., 2003; *Cochran et al*., 2009] have predicted and evidenced the reduction in the effective elastic shear modulus of the fault zone material related to intense damage. In specific relation to the EPF, the surface breaks at different sites associated with the 1997 Cariaco earthquake [*Audemard*, 2006] reveal possible damage related to previous events. Besides, earlier studies have shown the reduction in effective elastic moduli associated with reduction in seismic velocities [*Cochran et al*., 2009]. The EPF has been imaged as a low-velocity zone from the surface down to 14 km by use of seismic tomography [*Grosser et al*., 2001] and a reduced-velocity layer has been identified with a maximum depth of 5 km below the unconsolidated sediments of the village of Cariaco by use of deep seismic refraction [*Liuzzi et al*., 2006].

Our model suggests a much wider CZ than the $W = L/6$ ratio [*Barbot et al*., 2008]. Nonetheless, *Cochran et al*. [2009] reported that the differences may be related to intrinsic variations in the width of damage zones along the sections of the same fault. The width and depth extent of compliant fault zones are still under debate in the community [*Duan*, 2011]. Moreover, other factors there are not developed in this work, such as the highly porous and permeable fault gouge zone [*Lees and Malin*, 1990; *Byerlee*, 1993; *Unsworth et al*., 1997] and the brittle-plastic transition [*Scholz*, 1988], may be associated with development of CZs [*Chen and Freymueller*, 2002]. The CZ model also underlines the existence of substantial creep along the upper part of the EPF (0–12 km), with 12 mm/yr in the western segment and 10 mm/yr in the eastern segment. According to these results, the displacement is locked between 40% and 50%.

7.3. Distributed-Slip Model

To assert the idea of a partially locked fault in the upper segments, we determined a slip inversion along the EPF using a procedure based on fault patches. Our results point to a partial creep in the upper segments (0–12 km), but the discretization of segments in several patches suggests that the velocity is not uniform. We identify two main zones with reduced slip values: a first zone roughly 12 km wide and 8 km deep, close to Cumaná City, and a smaller second area south of the CAC0 site and 32 km west of Cariaco. The first and larger zone with reduced creep was not affected by the 1997 event, judging from the distribution of Cariaco aftershocks [*Baumbach et al*., 2004]. It corresponds rather to the surface rupture of the 17 January 1929, Cumaná earthquake, as documented by *Paige* [1930], *Rodríguez and Chacín*, 1996, and *Mocquet et al*. [1996], and probably to the rupture of the 1797 earthquake [*Audemard*, 2007]. This area may then correspond to an asperity that previously ruptured during the 1929 earthquake but probably ruptured during the 1797 event.

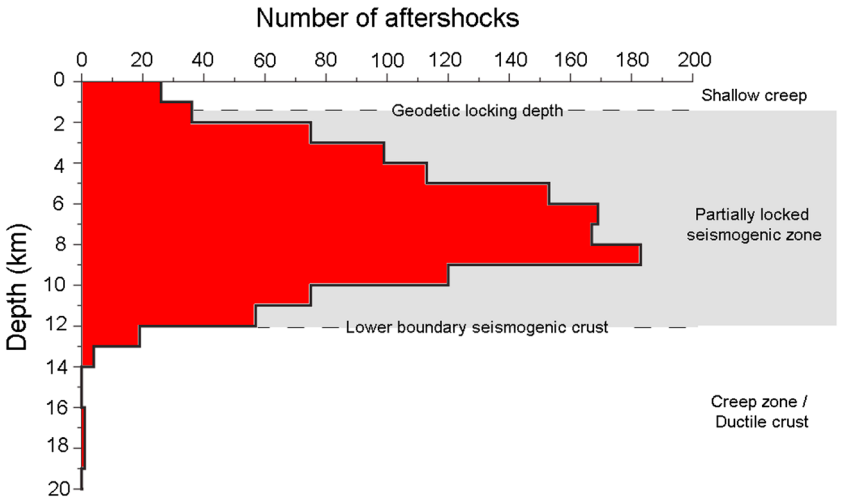

Figure 14. Distribution of 1997 Cariaco earthquake aftershocks [*Baumbach et al*., 2004] versus depth showing peak activity in the partially locked seismogenic zone. We show the hypothetic zones versus depth for the EPF according to the results of this work.

Despite the fact that the 1929 and 1997 ruptures may have completed the total length of a rather continuous and linear section [*Audemard*, 2006, 2007] and the EPF segment from the Caigüire Hills (Cumaná) to the Casanay-Guarapiche restraining bend has been considered as one subdivision of four segments that form the whole EPF [*Audemard et al*., 2000] our results indicate that this segment must be analyzed in at least two separate portions. Unfortunately, the major part of the western subdivision is underwater, precluding the observation of surface creep.

7.4. Displacement Simulation Method Using Nonvertical Dislocations

In this paper, we reevaluate the set of dislocations in a uniform elastic half-space applied to the EPF and proposed by *Jouanne et al*. [2011]. In the upgrade, we do not observe significant changes of relation with the displacement pattern. In fact, our preferred model shows two segments with four nonvertical dislocation planes, much as in the earlier work. We take into account the dislocations along the EPF that imply that the relative displacements for the Caribbean-South America plate boundary in the study zone are concentrated on the EPF. We reaffirm the idea of sizeable aseismic displacement along the upper part of the EPF with 40% and 50%, respectively, for the upper western and eastern segments.

8. Conclusions

Modeling from GNSS observations since 2003 has made possible the identification of creep in the upper part of the EPF. This conclusion is reinforced by the observation of progressively displaced markers [*Audemard*, 2006]. Additionally, the simple and asymmetric elastic half-space approaches indicate a shallow locking depth that suggests fault creep, and the compliant zone model and displacement-simulation method using nonvertical dislocations indicate between 40% and 50% of locked displacement between 12 km depth and the surface. As suggested by *Jouanne et al*. [2011], this behavior is probably related to either the existence of serpentinite lenses [*Moore et al*., 1997] or deep-seated fluid escape. The weathered serpentinites have been reported to form a narrow ridge separating two faults near Casanay [*Metz*, 1965]. The western portion of the western segment of the EPF corresponds to the segment affected by the 1929 event [*Audemard*, 2007] and the eastern segment is related more to the 1997 Cariaco earthquake [*Audemard*, 2006; *Jouanne et al*., 2011]. Moreover, from discretization of segments into several patches, we conclude that the interseismic slip is not uniform. We highlight a low-slip rate zone eastward of Cumaná City, roughly 12 km wide and 8 km deep and probably related to the rupture zone of the 1929 earthquake that may then correspond to an asperity along the fault. Nevertheless, creep or partial creep is present in both segments of the EPF. The postseismic afterslip of the 1997 event could help explain the creep in the eastern segment. For the western segment, the creep might be explained in several ways: a postseismic effect of the

1929 earthquake, after which the creep must have continued to decrease with time or as a consequence of a postseismic effect of the 1997 earthquake that affected another segment of the EPF. However, in a recent study *Audemard* [2011] revealed at least 13 events around M_s 7.0 (moderate earthquakes) in the past 5.6 kyr, representing an average return period of 430 years, which is significantly different from the 195 year return period estimated in the case of full locking of the upper 12 km of the EPF [*Jouanne et al*., 2011]. This observation supports the hypothesis of significant creep during interseismic periods and not only after major earthquakes. As a consequence, the observed creep cannot be interpreted as "classical" afterslip of a major earthquake. The seismicity distribution with depth could suggest the occurrence of shallow creep in the upper part, with a gradual transition to a partially locked seismogenic zone confined between 1.5 and 12 km, and the existence of ductile shear below 12 km (Figure 14).

From comparisons of fault-perpendicular velocity profiles and using the Fisher-Snedecor test of variances, we select the unconstrained parameters asymmetric model as the best model. This model is likely the best model from the statistical point of view than the other models. Nevertheless, field observations and the results of several models present the creep in the EPF as a significant issue to take into account. This development leads to the conclusion that the CZ model is a good model from the geological and geodetic points of view. Likewise, the CZ model is a better model, with more than a 70% confidence level, than the displacement simulation using the nonvertical dislocation model. The distributed-slip model was omitted from the comparison because the discretization of segments into patches generates a far lower degree of freedom, precluding comparison with the other models. Nonetheless, this model, with a quite good fit to the data, is based on the same EPF geometry as the CZ model.

Acknowledgments

The authors thank two anonymous reviewers and the Associate Editor for their helpful comments and suggestions. We thank Sylvain Barbot for his support with the STATICI code and for comments and recommendations. We are also grateful to Miguel Palma, Rafael Abreu, Leonardo Alvarado, and Donata Liuzzi (former coworker) from FUNVISIS and Carlos Mendoza (Centro de Geociencias, UNAM). The recent update of data in 2013 was made possible by the collaboration of Javier Oropeza, Walter Reategui, Alí Gómez, and Maxlimer Vallée from FUNVISIS; Lenin Ortega, Carlos Martínez, Pedro Oropeza, and Gustavo Rodríguez from PDVSA-INTEVEP; Annio Moreno from PDVSA Servicios; and Johana Bautista from IGVSB. We thank the "Coordinación Técnica de Geodesia"-IGVSB for the Cumaná station data. We are grateful to the Audemard family for allowing us to install the base camp and GNSS base station (AUD0). C. Reinoza's PhD thesis and stay at ISTerre Laboratory are funded through Venezuela's FUNDAYACUCHO grant 756514C. We thank the financial and logistic support offered by FUNVISIS and ISterre. This research is a contribution to FONACIT-ECOS Nord grants PI 2003000090 (French code V10U01) and PI-2009000818 and FONACIT-2002000478 (GEODINOS), and FONACIT-2012002202 (GIAME), and LabEx OSUG@2020.

References

Aggarwal, Y. (1983), Neotectonics of the southern Caribbean: Recent data, new ideas, *Acta Cientifica Venezolana*, *34*(1), 17.

Altamimi, Z., L. Métivier, and X. Collilieux (2012), ITRF2008 plate motion model, *J. Geophys. Res.*, *117*, B07402, doi:10.1029/2011JB008930.

Ambraseys, N. N. (1970), Some characteristic features of the Anatolian fault zone, *Tectonophysics*, *9*(2–3), 143–165, doi:10.1016/0040-1951(70)90014-4.

Audemard, F. A. (1993), Néotectonique, sismotectonique et aléa sismique du nord-ouest du Vénézuela (système de failles d'Oca-Ancón), PhD thesis, 369 pp., University of Montpellier II.

Audemard, F. A. (1997), Preliminary geological report on the Cariaco Earthquake July 09, 1997, Venezuela, *Int. Cent. Disaster-Mitigation Eng. Newsl.*, *6*(2), 7.

Audemard, F. A. (1998), Evolution géodynamique de la facade nord Sud-américaine: Nouveaux apports de l'histoire géologique du Bassin de Falcón, Vénézuéla, paper presented at XIV Caribbean Geological Conference, Trinidad.

Audemard, F. A. (1999a), El sismo de Cariaco del 09 de Julio de 1997, edo. Sucre, Venezuela: Nucleación y progresión de la ruptura a partir de observaciones geológicas, Proceedings, VI Congreso Venezolano de Sismología e Ingeniería Sísmica, Mérida, Venezuela (CD-ROM).

Audemard, F. A. (1999b), Nueva percepción de la sismicidad histórica del segmento en tierra de la falla de El Pilar. Venezuela nororiental. A partir de primeros resultados paleosísmicos, *Proceedings VI Congreso Venezolano de Sismología e Ingeniería Sísmica*, *Mérida*, 10.

Audemard, F. A. (2006), Surface rupture of the Cariaco July 09, 1997 earthquake on the El Pilar Fault, northeastern Venezuela, *Tectonophysics*, *424*(1–2), 19–39, doi:10.1016/j.tecto.2006.04.018.

Audemard, F. A. (2007), Revised seismic history of the El Pilar Fault. Northeastern Venezuela. From the Cariaco 1997 earthquake and recent preliminary paleoseismic results, *J. Seismol.*, *11*(3), 311–326.

Audemard, F. A. (2009), Key issues on the post-Mesozoic southern Caribbean plate boundary, in *Growth and Collapse of the Tibetan Plateau*, edited by R. Gloaguen, and L. Ratschbacher, *Geol. Soc. London Spec. Publ.*, *328*, 569–586, doi:10.1144/SP328.23.

Audemard, F. A. (2011), Multiple-trench investigations across the newly ruptured segment of the El Pilar Fault in northeastern Venezuela after the 1997 Cariaco earthquake, *Geol. Soc. Am. Spec. Pap.*, *479*, 133–157, doi:10.1130/2011.2479(06).

Audemard, F. A., M. N. Machette, J. W. Cox, R. L. Dart, and K. M. Haller (2000), Map of Quaternary faults of Venezuela, *U.S. Geol. Surv. Open File Rep.*, *00–0018*.

Audemard, F. A., G. Romero, H. Rendon, and V. Cano (2005), Quaternary fault kinematics and stress tensors along the southern Caribbean from fault-slip data and focal mechanism solutions, *Earth Sci. Rev.*, *69*(3–4), 181–233, doi:10.1016/j.earscirev.2004.08.001.

Audemard, F. A., et al. (2007), La depresión submarina de Guaracayal, estado Sucre, Venezuela: Una barrera para la propagación de la ruptura cosísmica a lo largo de la falla de El pilar, *Interciencia*, *32*, 735–741.

Barbot, S., Y. Fialko, and D. Sandwell (2008), Effect of a compliant fault zone on the inferred earthquake slip distribution, *J. Geophys. Res.*, *113*, B06404, doi:10.1029/2007JB005256.

Barbot, S., Y. Fialko, and D. Sandwell (2009), Three-dimensional models of elasto-static deformation in heterogeneous media, with applications to the Eastern California Shear Zone, *Geophys. J. Int.*, *179*, 500–520.

Baumbach, M., H. Grosser, G. Romero, J. Rojas, and M. Sobiesiak (1999), Aftershock studies of the July 9, 1997, Cariaco earthquake: American Geophysical Union 1999 Spring Meeting Boston: Eos (Transactions, American Geophysical Union), 80, 17, supplement S226, abstract S42A-01.

Baumbach, M., H. Grosser, G. Romero Torres, J. L. Rojas Gonzales, M. Sobiesiak, and W. Welle (2004), Aftershock pattern of the July 9, 1997 M_w=6.9, Cariaco earthquake in northeastern Venezuela, *Tectonophysics*, *379*(1–4), 1–23.

Beltrán, C., compiler (1993), Mapa neotectónico de Venezuela: Caracas, Venezuela, Fundación Venezolana de Investigaciones Sismológicas, scale 1:2,000,000.

Beltrán, C. (1994), Trazas activas y síntesis neotectónica de Venezuela a escala 1:2.000.000, in *Proceedings*, *7th Congreso Venezolano de Geofísica*: Caracas, pp. 541–547.

Beltrán, C., and C. Giraldo (1989), *Aspectos Neotectónicos de la Región Nororiental de Venezuela*, vol. 3, in, pp. 999–1021, VII Congreso Geológico Venezolano, Caracas, Venezuela, Barquisimeto.
Beltrán, C., A. Singer, and J. A. Rodríguez (1996), The El Pilar Fault active trace (northeastern Venezuela): Neotectonic evidences and paleoseismic data, in *Proceedings*, *3rd International Symposium on Andean Geodynamics*, pp. 153–156, Saint-Malo, France.
Ben-Zion, Y., and C. G. Sammis (2003), Characterization of fault zones, *Pure Appl. Geophys.*, *160*, 677–715, doi:10.1007/PL00012554.
Ben-Zion, Y., Z. Peng, D. Okaya, L. Seeber, J. G. Armbruster, N. Ozer, A. J. Michael, S. Baris, and M. Aktar (2003), A shallow fault-zone structure illuminated by trapped waves in the Karadere–Duzce branch of the North Anatolian Fault, western Turkey, *Geophys. J. Int.*, *152*(3), 699–717, doi:10.1046/j.1365-246X.2003.01870.x.
Beutler, G., M. Rothacher, S. Schaer, T. A. Springer, J. Kouba, and R. E. Neilan (1999), The International GNSS Service (IGS): An interdisciplinary service in support of Earth sciences, *Adv. Space Res.*, *23*, 631–653.
Bürgmann, R., D. Schmidt, R. M. Nadeau, M. d'Alessio, E. Fielding, D. Manaker, T. V. McEvilly, and M. H. Murray (2000), Earthquake potential along the northern Hayward Fault, California, *Science*, *289*(5482), 1178–1182, doi:10.1126/science.289.5482.1178.
Byerlee, J. (1993), Model for episodic flow of high-pressure water in fault zones before earthquakes, *Geology*, *21*, 303–306.
Chen, Q., and J. T. Freymueller (2002), Geodetic evidence for a near-fault compliant zone along the San Andreas Fault in the San Francisco Bay Area, *Bull. Seismol. Soc. Am.*, *92*(2), 656–671.
Chéry, J. (2008), Geodetic strain across the San Andreas Fault reflects elastic plate thickness variations (rather than fault slip rate), *Earth Planet. Sci. Lett.*, *269*, 352–365.
Chester, F. M., and J. S. Chester (1998), Ultracataclasite structure and friction processes of the Punchbowl Fault, San Andreas system, California, *Tectonophysics*, *295*, 199–221, doi:10.1016/S0040-1951(98)00121-8.
Chester, J. S., F. M. Chester, and A. K. Kronenberg (2005), Fracture surface energy of the Punchbowl fault, San Andreas system, *Nature*, *437*(7055), 133–136.
Chinnery, M. A. (1961), The deformation of the ground around surface faults, *Bull. Seismol. Soc. Am.*, *51*(3), 355–372.
Christeson, G. L., P. Mann, A. Escalona, and T. J. Aitken (2008), Crustal structure of the Caribbean–northeastern South America arc-continent collision zone, *J. Geophys. Res.*, *113*, B08104, doi:10.1029/2007JB005373.
Clark, S. A., C. A. Zelt, M. B. Magnani, and A. Levander (2008), Characterizing the Caribbean-South American plate boundary at 64°W using wide-angle seismic data, *J. Geophys. Res.*, *113*, B07401, doi:10.1029/2007JB005329.
Cochran, E., Y.-G. Li, P. Shearer, S. Barbot, Y. Fialko, and J. Vidale (2009), Seismic and geodetic evidence for extensive, long-lived fault damage zones, *Geology*, *37*(4), 315–318.
Dach, R., and P. Walser (2013), Bernese GPS software, Version. 5.2, Astronomical Institute, University of Bern.
DeMets, C., P. E. Jansma, G. S. Mattioli, T. H. Dixon, F. Farina, R. Bilham, E. Calais, and P. Mann (2000), GPS geodetic constraints on Caribbean-North America plate motion, *Geophys. Res. Lett.*, *27*(3), 437–440, doi:10.1029/1999GL005436.
Diao, F., X. Xiong, R. Wang, Y. Zheng, and H. Hsu (2010), Slip model of the 2008 M_w 7.9 Wenchuan (China) earthquake derived from the coseismic GPS data, *Earth Planets Space*, *62*, 869–874.
Diao, F., X. Xiong, and R. Wang (2011), Mechanisms of transient postseismic deformation following the 2001 M_w 7.8, Kunlun (China) Earthquake, *Pure Appl. Geophys.*, *168*(5), 767–779, doi:10.1007/s00024-010-0154-5.
Dor, O., Y. Ben-Zion, T. Rockwell, and J. Brune (2006), Pulverized rocks in the Mojave section of the San Andreas Fault zone, *Earth Planet. Sci. Lett.*, *245*, 642–654.
Duan, B. (2011), Reply to comment by Y. Fialko on "Deformation of compliant fault zones induced by nearby earthquakes: Theoretical investigations in two dimensions", *J. Geophys. Res.*, *116*, B12302, doi:10.1029/2011JB008567.
Faulkner, D., A. Lewis, and E. Rutter (2003), On the internal structure and mechanics of large strike-slip faults: Field observations from the Carboneras Fault, southeastern Spain, *Tectonophysics*, *367*, 235–251.
Fialko, Y. (2004), Probing the mechanical properties of seismically active crust with space geodesy: Study of the co-seismic deformation due to the 1992 M_w7.3 Landers (Southern California) earthquake, *J. Geophys. Res.*, *109*, B03307, doi:10.1029/2003JB002756.
Fialko, Y., D. Sandwell, D. Agnew, M. Simons, P. Shearer, and B. Minster (2002), Deformation on nearby faults induced by the 1999 Hector Mine earthquake, *Science*, *297*(5588), 1858–1862.
Fulton, P. M., G. Schmalzle, R. N. Harris, and T. Dixon (2010), Reconciling patterns of interseismic strain accumulation with thermal observations across the Carrizo segment of the San Andreas Fault, *Earth Planet. Sci. Lett.*, *300*(3–4), 402–406, doi:10.1016/j.epsl.2010.10.024.
González, J., M. Schmitz, F. A. Audemard, R. Contreras, A. Mocquet, J. Delgado, and F. De Santis (2004), Site effects of the 1997 Cariaco, Venezuela earthquake, *Eng. Geol.*, *72*, 143–177.
Grosser, H., A. Rietbrock, M. Baumbach, G. Romero Torres, and J. Rojas (2001), Seismic tomography in the aftershock region of the Cariaco earthquake 1997, *Eos Trans. AGU, 82*(47), Fall Meet. Suppl., Abstract S32E-03.
Hamiel, Y., and Y. Fialko (2007), Structure and mechanical properties of faults in the north Anatolian fault system from InSAR observations of coseismic deformation due to the 1999 Izmit (Turkey) earthquake, *J. Geophys. Res.*, *112*, B07412, doi:10.1029/2006JB004777.
Hernández, G., T. Rossi, J. F. Stephan, and R. Blanchet (1987), Etude géologique de la Serrania del Interior Oriental (Venezuela) sur le transect Cariaco-Maturin, *Oil Gas Sci. Technol.-Rev.*, IFP, *42*(1), 3–30.
Houlié, N., and B. Romanowicz (2011), Asymmetric deformation across the San Francisco Bay area faults from GPS observations in Northern California, *Phys. Earth Planet. Inter.*, *184*, 143–153.
Hugentobler, U., et al. (2001), Bernese GPS software, Version 4.2, University of Bern.
Jacome, M. I., N. Kusznir, and S. Flint (1999), Structural and isostatic modelling of Serranía del Interior thrust belt and Monagas foreland basin: Eastern Venezuela. Fourth International Symposium on Andean Geodynamics Göttingen (Germany), Oct. 4–6, pp. 367–371. Extended abstract.
Jolivet, R., R. Cattin, N. Chamot-Rooke, C. Lasserre, and G. Peltzer (2008), Thin-plate modelling of interseismic deformation and asymmetry across the Altyn Tagh Fault zone, *Geophys. Res. Lett.*, *35*, L02309, doi:10.1029/2007GL031511.
Jolivet, R., R. Bürgmann, and N. Houlié (2009), Geodetic exploration of the elastic properties across and within the northern San Andreas Fault zone, *Earth Planet. Sci. Lett.*, *288*, 126–131.
Jouanne, F., F. A. Audemard, C. Beck, A. Van Welden, R. Ollarves, and C. Reinoza (2011), Present-day deformation along the El Pilar Fault in eastern Venezuela: Evidence of creep along a major transform boundary, *J. Geodyn.*, *51*(5), 398–410, doi:10.1016/j.jog.2010.11.003.
Kachanov, L. (1986), *Introduction to Continuum Damage Mechanics*, Martinus Nijhoff, Dordrecht, Netherlands.
King, G., and C. Nostro (1999), Almond Lite v. 2.02: A program to calculate Coulomb stresses around rectangular faults or dykes, Manual d'Utilisation, Institute de Phisique du Globe, Paris.
Le Pichon, X., C. Kreemer, and N. Chamot-Rooke (2005), Asymmetry in elastic properties and the evolution of large continental strike-slip faults, *J. Geophys. Res.*, *110*, B03405, doi:10.1029/2004JB003343.

Lees, J. M., and P. E. Malin (1990), Tomographic images of *P*-wave velocity variation, California, *J. Geophys. Res.*, *95*, 21,793–21,804, doi:10.1029/JB095iB13p21793.
Li, Y., J. Vidale, K. Aki, C. Marone, and W. Lee (1994), Fine-structure of the Landers fault zone—Segmentation and the rupture process, *Science*, *265*, 367–370.
Lindquist, K., K. Engle, D. Stahlke, and E. Price (2004), Global topography and bathymetry grid improves research efforts, *Eos Trans. AGU*, *85*(19), 186, doi:10.1029/2004EO190003. [Available at http://www.agu.org/pubs/crossref/2004/2004EO190003.shtml.]
Liuzzi, D., M. Schmitz, M. Jácome, and J. Sánchez (2006), Adelgazamiento de sedimentos Cretácicos-Oligocenos bajo la Serranía del Interior, Noreste de Venezuela: Evidencia a partir de observaciones de sísmica profunda, IX Simposio Bolivariano de Exploración Petrolera en las Cuencas Subandinas, Cartagena, Colombia. CD. 1–8.
Lyakhovsky, V., Y. Ben-Zion, and A. Agnon (2001), Earthquake cycle, fault zones, and seismicity patterns in a rheologically layered lithosphere, *J. Geophys. Res.*, *106*, 4103–4120, doi:10.1029/2000JB900218.
Lyons, S. N., Y. Bock, and D. T. Sandwell (2002), Creep along the Imperial Fault, Southern California, from GPS measurements, *J. Geophys. Res.*, *107*(B10), 2249, doi:10.1029/2001JB000763.
Malservisi, R., K. P. Furlong, and T. H. Dixon (2001), Influence of the earthquake cycle and lithospheric rheology on the dynamics of the Eastern California shear zone, *Geophys. Res. Lett.*, *28*(14), 2731–2734, doi:10.1029/2001GL013311.
Melbourne, W. G. (1985), The case for ranging in GPS based geodetic systems, in *Proceedings of the First International Symposium on Precise Positioning with the Global Positioning System*, edited by C. Goad, pp. 373–386, U.S. Dep. of Commer., Rockville, Md.
Mendoza, C. (2000), Rupture history of the 1997 Cariaco, Venezuela, earthquake from teleseismic *P* waves, *Geo phys. Res. Lett.*, *27*(10), 1555–1558, doi:10.1029/1999GL011278.
Metz, H. (1965), Geology of the El Pilar Fault zone. state of Sucre, Venezuela, *IV Caribbean Geological Conference*, Trinidad, pp. 293–298.
Minster, J., and T. H. Jordan (1978), Present-day plate motions, *J. Geophys. Res.*, *83*(B11), 5331–5354, doi:10.1029/JB083iB11p05331.
Mocquet, A., C. Beltrán, M. Lugo, J. A. Rodriguez, and A. Singer (1996), Seismological interpretation of the historical data related to the 1929 Cumaná earthquake, Venezuela, *Third International Symposium on Andean Geodynamics*, Saint-Malo (France), Sept. 17–19, 203–206. Extended abstract.
Molnar, P., and L. Sykes (1969), Tectonics of the Caribbean and Middle America regions from focal mechanisms and seismicity, *Geol. Soc. Am. Bull.*, *80*, 1639–1684, doi:10.1130/0016-7606(1969)80[1639:TOTCAM]2.0.CO;2.
Moore, D., D. A. Lockner, M. Shengli, R. Summers, and J. Byerlee (1997), Strengths of serpentinite gouges at elevated temperatures, *J. Geophys. Res.*, *102*(B7), 14,787–14,801, doi:10.1029/97JB00995.
Motagh, M., R. Wang, T. R. Walter, R. Bürgmann, E. Fielding, J. Anderssohn, and J. Zschau (2008), Coseismic slip model of the 2007 August Pisco earthquake (Peru) as constrained by Wide Swath radar observations, *Geophys. J. Int.*, *174*(3), 842–848, doi:10.1111/j.1365-246X.2008.03852.x.
Motagh, M., B. Schurr, J. Anderssohn, B. Cailleau, T. R. Walter, R. Wang, and J.-P. Villotte (2010), Subduction earthquake deformation associated with 14 November 2007, M_w 7.8 Tocopilla earthquake in Chile: Results from InSAR and aftershocks, *Tectonophysics*, *490*(1–2), 60–68, doi:10.1016/j.tecto.2010.04.033.
Okada, Y. (1985), Surface deformation due to shear and tensile faults in a half-space, *Bull. Seismol. Soc. Am.*, *75*(4), 1135–1154.
Oskin, M., and A. Iriondo (2004), Large-magnitude transient strain accumulation on the Blackwater Fault, Eastern California shear zone, *Geology*, *32*, 313–316.
Ostini, L., R. Dach, M. Meindl, S. Schaer, and U. Hugentobler (2008), *FODITS*: A new tool of the Bernese GPS software, in *Proceedings of EUREF 2008 Symposium*, edited by J. A. Torres and H. Hornik, Brussels, Belgium.
Paige, S. (1930), The earthquake at Cumaná, Venezuela, January 17, 1929, *Bull. Seismol. Soc. Am.*, *20*, 1–10.
Palma, M., F. Audemard, and G. Romero (2010), New focal mechanism solutions for Venezuela and neighbouring areas 2005–2008: Importance of the National Seismological Network's density and distribution, *Rev. Téc. Ing. Univ. Zulia*, *33*, 1–14.
Peng, Z., and Y. Ben-Zion (2006), Temporal changes of shallow seismic velocity around the Karadere-Duzce branch of the north Anatolian Fault and strong ground motion, *Pure Appl. Geophys.*, *163*, 567–600.
Pérez, O. J. (1998), Seismological report on the M_w = 6.8 strong shock of 9 July 1997 in Cariaco, northeastern Venezuela, *Bull. Seismol. Soc. Am., Short Notes*, *23*(2), 101–106.
Pérez, O. J., and Y. P. Aggarwal (1981), Present-day tectonics of the southeastern Caribbean and northeastern Venezuela, *J. Geophys. Res.*, *86*(B11), 10,791–10,804, doi:10.1029/JB086iB11p10791.
Pérez, O. J., R. Bilham, R. Bendick, J. R. Velandía, N. Hernández, C. Moncayo, M. Hoyer, and M. Kozuch (2001a), Velocity field across the southern Caribbean plate boundary and estimates of Caribbean/South-American plate motion using GPS geodesy 1994–2000, *Geophys Res Lett*, *28*, doi:10.1029/2001GL013183.
Pérez, O. J., R. Bilham, R. Bendick, N. Hernández, M. Hoyer, J. R. Velandia, C. Moncayo, and M. Kozuch (2001b), Velocidad relativa entre las placas del Caribe y Sudamérica a partir de observaciones dentro del sistema de posicionamiento global (GPS) en el norte de Venezuela, *Interciencia*, *26*(2), 69–74.
Pindell, J., and L. Kennan (2007), Cenozoic kinematics and dynamics of oblique collision between two convergent plate margins: The Caribbean–South America collision in eastern Venezuela, Trinidad and Barbados, in *The Paleogene of the Gulf of Mexico and Caribbean Basins; Processes, Events, and Petroleum Systems*, Proceedings, 27th Bob F. Perkins Research Conference, Gulf Coast Section of the Society of Economic Paleontologists and Mineralogists, edited by L. Kennan, J. Pindell, and N. Rosen, pp. 458–553, Society of Economic Paleontologists and Mineralogists, Houston, Tex.
Rodríguez, J. A., and C. A. Chacín (1996), Contribución al estudio del sismo de Cumaná año 1929. Compilación y notas, *Bol. Hist. Geocienc. Venez.*, *2*, 1–77.
Romero, G., F. A. Audemard, H. Rendón, and N. Orihuela (2002), Mapa de Soluciones Focales de Sismos Sentidos en Venezuela y Regiones Vecinas entre 1957 y 2002, *Edición Conmemorativa XXX Aniversario de FUNVISIS*, Caracas, FUNVISIS, scale ~1:2,450,000.
Savage, J. C., and R. O. Burford (1973), Geodetic determination of relative plate motion in central California, *J. Geophys. Res.*, *78*, 832–845, doi:10.1029/JB078i005p00832.
Schmalzle, G., T. Dixon, R. Malservisi, and R. Govers (2006), Strain accumulation across the Carrizo segment of the San Andreas Fault, California: Impact of laterally varying crustal properties, *J. Geophys. Res.*, *111*, B05403, doi:10.1029/2005JB003843.
Scholz, C. H. (1988), The brittle-plastic transition and the depth of seismic faulting, *Geol. Rundsch.*, *77*, 319–328.
Schubert, C. (1984), Basin formation along the Bocono-Moron-El Pilar fault system, Venezuela, *J. Geophys. Res.*, *89*(B7), 5711–5718, doi:10.1029/JB089iB07p05711.
Singer, A., and F. A. Audemard (1997), Aportes de Funvisis al desarrollo de la geología de fallas activas y de la paleosismología para los estudios de amenaza y riesgo sísmico, in *Diseño Sismorresistente: Especificaciones y Criterios Empleados en Venezuela*, vol. 33, edited by J. Grases, pp. 25–38, Academia de las Ciencias Naturales, Matemáticas y Físicas Publicación Especial, Caracas, Venezuela.

Smith-Konter, B., D. Sandwell, and P. Shearer (2011), Locking depths estimated from geodesy and seismology along the San Andreas Fault System: Implications for seismic moment release, *J. Geophys. Res.*, *116*, B06401, doi:10.1029/2010JB008117.

Soulas, J.-P. (1986), Neotectónica y tectónica activa en Venezuela y regiones vecinas, *Proceedings of 6th Congreso Geológico Venezolano* (1985): Caracas, Venezuela, 10, 6639–6656.

Speed, R., R. Russo, J. Weber, and K. C. Rowley (1991), Evolution of southern Caribbean plate boundary, vicinity of Trinidad and Tobago, *Am. Assoc. Pet. Geol. Bull.*, *75*(11), 1789–1794.

Stephan, J.-F. (1982), Evolution Géodinamique du Domaine Caraïbe, Andes et Chaîne Caraïbe sur la Transversale de Barquisimeto (Vénézuéla) [Ph.D. thesis]: Brest, France, Université de Bretagne Occidentale, 512 pp.

Thurber, C., S. Roecker, K. Roberts, M. Gold, L. Powell, and K. Rittger (2003), Earthquake locations and three-dimensional fault zone structure along the creeping section of the San Andreas Fault near Parkfield, CA: Preparing for SAFOD, *Geophys Res Lett*, *30*(3), 1112, doi:10.1029/2002GL016004.

Turcotte, D., W. Newman, and R. Shcherbakov (2003), Micro and macroscopic models of rock fracture, *Geophys. J. Int.*, *152*, 718–728.

Unsworth, M. J., P. E. Malin, G. D. Egbert, and J. R. Booker (1997), Internal structure of the San Andreas Fault at Parkfield California, *Geology*, *25*, 359–362.

Van Daele, M., et al. (2011), Reconstruction of Late-Quaternary sea- and lake-level changes in a tectonically active marginal basin using seismic stratigraphy: The Gulf of Cariaco, NE Venezuela, *Mar. Geol.*, *279*(1–4), 37–51, doi:10.1016/j.margeo.2010.10.011.

Vierbuchen, R. C. (1984), The geology of the El Pilar fault zone and adjacent areas in northeastern Venezuela, in *The Caribbean–South America Boundary and Regional Tectonics*, edited by W. E. Bonini, R. B. Hargraves, and R. Shagam, pp. 189–212, Geol. Soc. Am. Mem., Boulder, Colo.

Wang, L., R. Wang, F. Roth, B. Enescu, S. Hainzl, and S. Ergintav (2009), Afterslip and viscoelastic relaxation following the 1999 M 7.4 İzmit earthquake from GPS measurements, *Geophys. J. Int.*, *178*(3), 1220–1237, doi:10.1111/j.1365-246X.2009.04228.x.

Wang, R., B. Schurr, C. Milkereit, Z. Shao, and M. Jin (2011), An improved automatic scheme for empirical baseline correction of digital strong-motion records, *Bull. Seismol. Soc. Am.*, *101*(5), 2029–2044, doi:10.1785/0120110039.

Wang, R., S. Parolai, M. Ge, M. Jin, T. R. Walter, and J. Zschau (2013), The 2011 M_w 9.0, Tohoku earthquake: Comparison of GPS and strong-motion data, *Bull. Seismol. Soc. Am.*, *103*(2B), 1336–1347, doi:10.1785/0120110264.

Wdowinski, S. (2009), Deep creep as a cause for the excess seismicity along the San Jacinto Fault, *Nat. Geosci.*, *2*, 882–885.

Weber, J. C., T. H. Dixon, C. DeMets, W. B. Ambeh, P. Jansma, G. Mattioli, J. Saleh, G. Sella, R. Bilham, and O. Pérez (2001), GPS estimate of relative motion between the Caribbean and South American Plates, and geologic implications for Trinidad and Venezuela, *Geology*, *29*(1), 75–78, doi:10.1130/0091-7613.

Weber, J. C., J. Saleh, S. Balkaransingh, T. Dixon, W. Ambeh, T. Leong, A. Rodriguez, and K. Miller (2011), Triangulation-to-GPS and GPS-to-GPS geodesy in Trinidad, West Indies: Neotectonics, seismic risk, and geologic implications, *Mar. Pet. Geol.*, *28*(1), 200–211, doi:10.1016/j.marpetgeo.2009.07.010.

Weertman, J., and J. Weertman (1964), *Elementary Dislocation Theory*, pp. 213, Macmillan, New York.

Wilson, B., T. Dewers, Z. Reches, and J. Brune (2005), Particle size and energetics of gouge from earthquake rupture zones, *Nature*, *434*(7034), 749–752.

Wübbena, G. (1985), Software development for geodetic positioning with GPS using TI 4100 code and carrier measurements, in *Proc. of First Int. Sym. on Precise Position With GPS Rockville*, edited by C. C. Goad, pp. 403–412, Maryland.

Xu, C., Y. Liu, Y. Wen, and R. Wang (2010), Coseismic slip distribution of the 2008 M_w 7.9, Wenchuan earthquake from joint inversion of GPS and InSAR data, *Bull. Seismol. Soc. Am.*, *100*(5B), 2736–2749, doi:10.1785/0120090253.